Chapter 2

Active and Tunable Metamaterials

Yongjun Huang, Jian Li and Guangjun Wen

Additional information is available at the end of the chapter

http://dx.doi.org/10.5772/67198

Abstract

In this chapter, we will first present the research progress on the active and tunable metamaterials based on different realization methods, such as varactor diodes, liquid crystals, superconductivity, and structural-shifting structures. Then we focus on the achievements in our research group for the tunable metamaterials by using the ferrite as the substrate of metamaterials. We will present the designs and theories of single-, dual-, and triple-band tunable metamaterials based on the ferrite and the design of metamaterial absorbers based on the ferrite. It will indicate that the proposed tunable metamaterials have many advantages compared with other active and tunable metamaterials.

Keywords: tunable metamaterials and absorbers, ferrite

1. Introduction

Metamaterial [1] is a kind of artificial material. When the unit cell of a metamaterial is much smaller than the working wavelength, it can be considered as a homogeneous medium. Metamaterial exhibits many novel electromagnetic properties [2–7] and has important potential applications [8–12], and has attracted wide research attention. However, there are many unsolved problems and bottlenecks, including the large loss, narrow bandwidth, and untunable frequency band. The active tunable metamaterials have shown novel advantages for solving the issues that appeared in the conventional metamaterial.

Here we conclude the recently developed active and tunable metamaterials based on the varactor diodes, liquid crystals, superconductivity, and structural-shifting structures. First, the tunable metamaterial based on the varactor diodes is proposed by Gil et al. [13] and Velez et al. [14]. As shown in **Figure 1(a)**, the diodes are integrated in the regular split ring resonators (SRRs), the resonance of the structure can be adjusted by controlling the DC bias acting

on the diodes. After that, various magnetic negative metamaterials and negative index metamaterials based on such varactor diodes are reported and experimentally demonstrated. For instances, researchers experimentally verified that the refractive index of S-shaped metamaterial loaded with diodes (**Figure 1b**) can be changed via altering the magnitude of DC bias [15]. By investigating one SRR unit loaded with a capacitor located at different position or loaded with capacitor with different capacitances (**Figure 1c**), the resonance can also be shifted [16]. Another similar design is achieved by integrating the BST capacitor into the SRR as shown in **Figure 1(d)** [17]. This kind of design can be flexibly integrated in the regular microstrip circuits to achieve the tunable band-pass/band-stop filters, antennas, and nonlinear devices [18, 19].

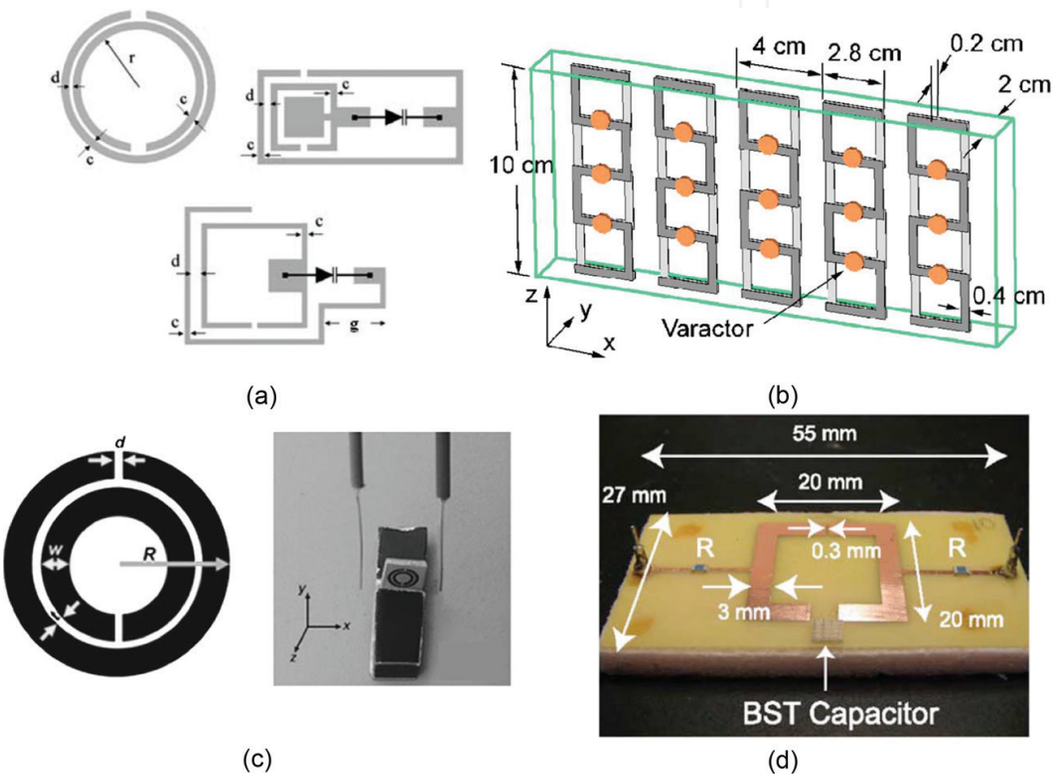

Figure 1. Tunable metamaterials based on varactor diodes. (a) SRR loaded with diodes [13], (b) S-shaped resonator loaded with diodes [15], (c) SRR loaded with capacitor [16], and (d) SRR loaded with BST capacitor [17].

It is well known that the dielectric permittivity of liquid crystal can be adjusted by changing the magnitude and direction of external electric field and magnetic field, and/or the temperature [20, 21]. Therefore, one can integrate the liquid crystal into the conventional metamaterials to realize the tunable designs. For example, researchers experimentally investigated the SRR and Omega-shaped magnetic negative metamaterials infiltrated with the liquid crystals as shown in **Figure 2(a)** and **(b)** [22, 23]. Then the tunability is achieved by controlling the direction of external magnetic field. At the same time, other researcher exhibited a similar SRR magnetic negative metamaterials loaded with the liquid crystals (see **Figure 2c**) and the tunability is obtained by changing the external electric field strengths [24]. At higher operating frequencies, it works as well for the liquid crystal-based tunable metamaterials. Researchers

numerically investigated the reconfigurable index of refraction from negative through zero to positive values by changing equivalently the index of liquid crystal for the kind of tunable metamaterial operating at near-infrared wavelength [25], as shown in **Figure 2(d)**. Another tunable fishnet metamaterials infiltrated by liquid crystals operated at optical ranges was numerically demonstrated as well recently as shown **Figure 2(e)** [26]. It has shown that the liquid crystal can be used to realize the tunable metamaterials and several external control methods can adjust and tune the properties of such metamaterials. However, the tuning range is not wide enough as observed in the previously mentioned references.

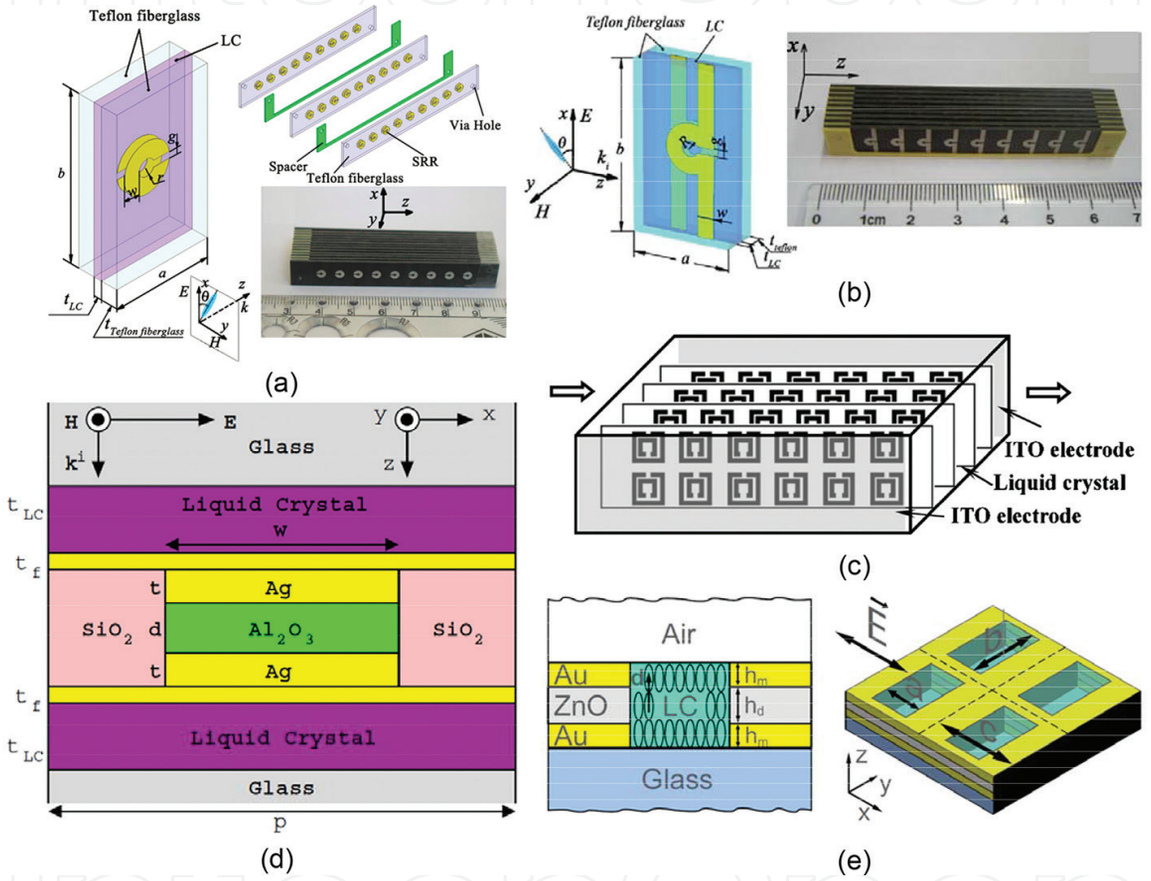

Figure 2. Tunable metamaterials based on liquid crystals. (a) Circular SRR structure [22], (b) Omega-shaped resonator [23], (c) square SRR structure [24], (d) near-infrared structure [25], and (e) fishnet structure [26].

Recently, other kinds of tunable metamaterials were also proposed by using, e.g., superconductivity and MEMS structures [27, 28] as shown in **Figure 3(a)** and **(b)**. For the superconductivity-based metamaterial, the tunability is obtained by changing the external DC or RF magnetic field [27]. For the MEMS metamaterial, the tunability is achieved by heating the nanostructure with rapid thermal annealing method to alter the direction of the SRR [28]. Another two similar structurally shifted metamaterials operated at microwave and THz range are shown in **Figure 3(c)** and as well, and these two designs can alter the electromagnetic responses by mechanically changing the relative positions for part of the SRRs in the array vertically and/or horizontally [29, 30].

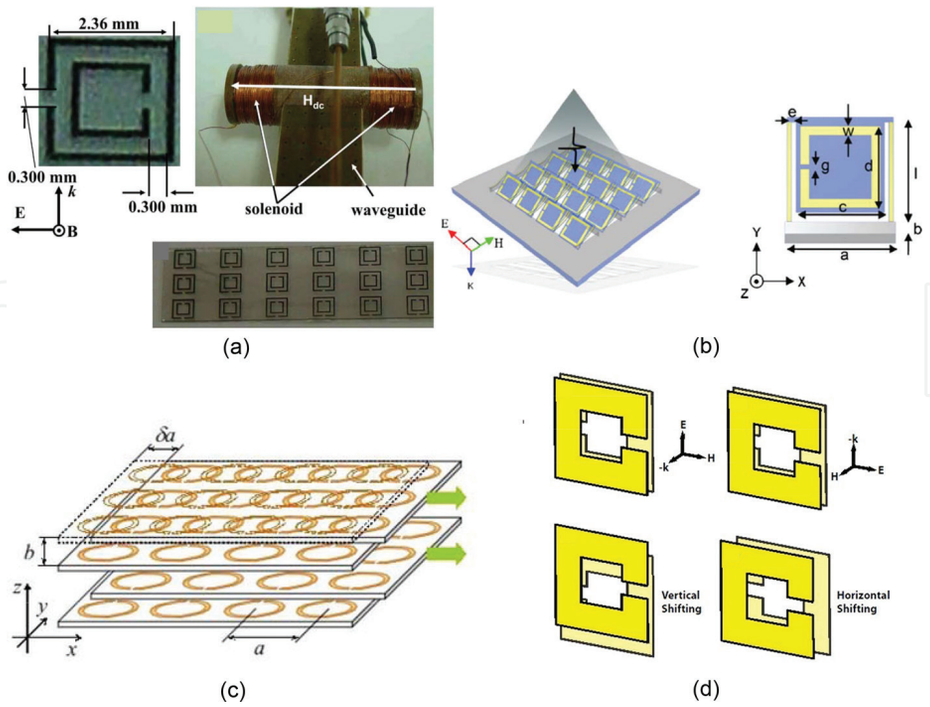

Figure 3. Other tunable metamaterial configurations. (a) Superconductivity [27], (b) MEMS [28], (c) structural shifted structure [29], and (d) THz structural shifted structure [30].

On the other hand, some researchers proposed ferrite-based metamaterials, that is, substituting ferrites such as yttrium iron garnets (YIG) for the SRR structures to obtain the negative permeability [31–38]. Dewar first proposed the ferrite-based metamaterial as shown in **Figure 4(a)** and gave the theoretical expressions of the effective parameters and analyzed the interactions of the ferrites and wires [31, 32]. Rachford et al. and Cai et al. numerically investigated the electromagnetic wave propagation properties of such metamaterials [33, 34] with minor modification (see **Figure 4b**) for the easy fabrication. He et al. and Zhao et al. fabricated the metamaterial samples and investigated experimentally the negative transmission and tunability characteristics [35, 36] at different frequencies as shown in **Figure 4(c)** and **(d)**. In our previous works, we also analyzed the theoretical parameters, investigated the negative refractive index characteristics, and discussed the different refractive characteristics in a broad frequency band [37, 38].

Similarly, due to the magnetic properties of the ferrites, it can be controlled with the applied DC field. The ferrites can be embedded into the conventional resonant structure metamaterials in order to realize the tunability. The experimental studies on the SRR metamaterial loaded with ferrite was carried out. The tunable characteristics of working frequency band for the single magnetic negative metamaterial and the double negative metamaterials are demonstrated as shown in **Figure 5(a)** and **(b)** [39, 40]. Our research has also shown that the ferrite embedded into the conventional metamaterials can not only realize the tunable frequency band, but also can realize the dual or even tri-band tunable characteristics (as shown in **Figure 5c**) [41]. This will be discussed in details in the next section. At the same time, researches used two different kinds of ferrites to realize the tunable dual-band metamaterials (as shown in **Figure 5d**) [42]. This realization process is simple, and its working frequency band can be adjusted in a wide frequency band with the applied DC magnetic field.

http://dx.doi.org/10.5772/67198

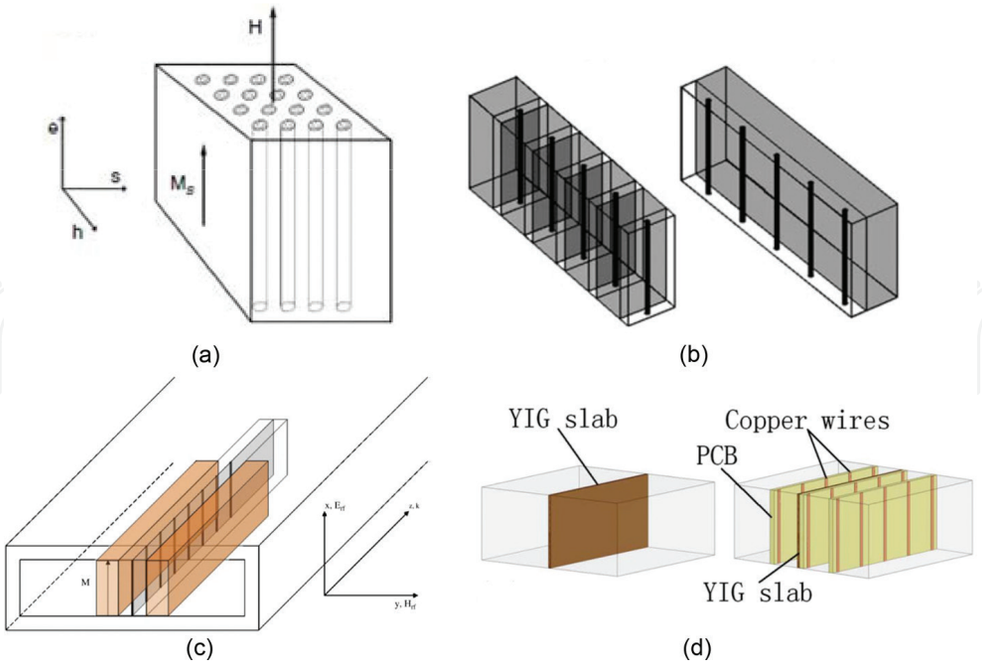

Figure 4. Tunable metamaterials based on the ferrite. (a) Original design [31, 32], (b) modification achievements [34], and (c and d) experimental demonstrations [35, 36].

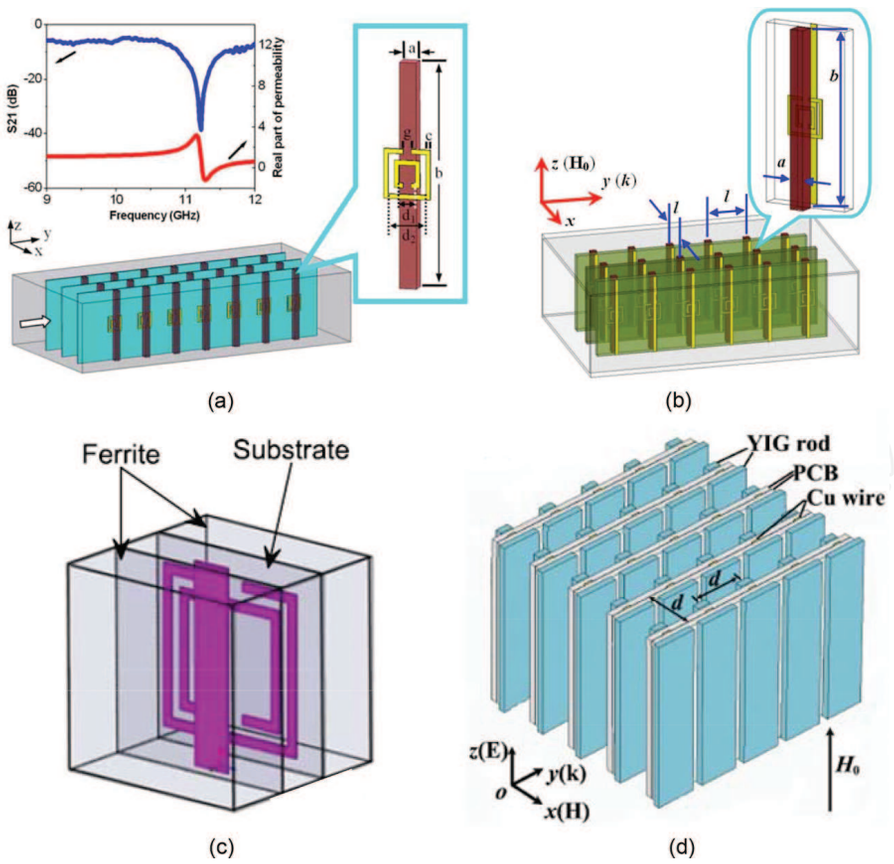

Figure 5. Tunable metamaterials loaded with ferrite as the substrate. (a) Magnetic negative structure [39], (b) double negative structure [40], and (c and d) dual-band structures [41, 42].

2. Theoretical analysis

Here the theoretical analysis of the proposed ferrite-inspired metamaterials is presented. As shown in **Figure 6(a)**, when a transverse electromagnetic (TEM) wave acts on the ferrite slabs along the *y*-axis (the electric field along the *z*-axis), and a DC magnetic bias acts on the ferrite slabs along the *z*-axis, the effective permeability of ferrite has the following property: $\mu_{\text{eff}} = (\mu^2 - \kappa^2)/\mu$, where $\mu = 1 + \omega_m\omega_0/(\omega_0^2 - \omega^2)$, $\kappa = \omega_m\omega/(\omega_0^2 - \omega^2)$ [43], and $\omega_0 = \gamma H_0$ stands for ferromagnetic resonance (FMR) frequency, γ denotes the gyromagnetic ratio, $\omega_m = 4\pi Ms\gamma$ represents the characteristic frequency of the ferrite slabs, ω is the angular frequency, and H_0 indicates the DC magnetic bias. For the ferrite slabs used here (TT1-3000 series of Trans-Tech Ltd., the saturation magnetization $4\pi Ms$ = 3000 G, ε_r = 12.9, tan δ = 0.0005, and resonance beamwidth ΔH = 228 Oe), the damping describing loss of ferrite should be taken into consideration. In that case, the FMR frequency can be revised to $\omega_0 + j\alpha\omega$, where α stands for the damping of the ferromagnetic precession. As a result, the effective permeability has changed to

$$\mu_{\text{eff}} = 1 - \frac{\omega_m}{\frac{\omega^2}{\omega_0 + \omega_m} - \omega_0 - j\alpha\omega\frac{\omega^2}{(\omega_0 + \omega_m)^2 + 1}} \quad (1)$$

The higher order infinitesimal α is usually ignored due to the very low loss in ferrite slabs.

The effective permeability is calculated under different magnetic biases based on Eq. (1), as shown in **Figure 6(b)**. It can be seen that the effective permeability of ferrite slabs exhibits all typical resonant characteristics with different DC magnetic biases. The negative Re(μ_{eff}) is achieved above the resonant frequencies. For one condition as an example, the Re(μ_{eff}) is negative in the frequency range of 9.5–14 GHz and changes to positive after 15 GHz when H_0 = 2.2 kOe. So, when combining the ferrite slabs into the classic magnetic metamaterial structures which exhibit negative permeability frequency band below or above the negative band of ferrite slabs, one can expect to achieve two negative Re(μ_{eff}) frequency band. On the other hand, for the continuous wires of the classic SRR-wires [2] and short wire pairs [44] structures (the Ω-like structures [45] can be also considered as continuous wires), the negative permittivity frequency band is wide enough which can cover the two negative permeability frequency bands. Therefore, the ferrite-based metamaterials have the ability to achieve the dual-band negative refractive index properties.

Moreover, as shown in **Figure 6(b)**, the magnetic resonant frequency of ferrite slabs is shifted from 9.5 to 12 GHz when H_0 increases from 2.2 to 3 kOe. So the negative permeability frequency band of ferrite slabs can be shifted arbitrarily and reversibly by controlling the magnetic bias. Furthermore, as shown in **Figure 6(b)**, the positive part of Re(μ_{eff}) is decreased when increasing of the magnetic bias. So the resonance frequencies of the SRR, Ω-like resonators and short wire pairs can be altered, resulting in the changing of the second operating band. Then we numerically investigate the above-mentioned three types of dual-band metamaterial to demonstrate the theoretical expectations. We also investigate the tunable triple-band realization and a single-band THz ferrite-based tunable metamaterials. Lastly, by using the ferrite, we propose two kinds of tunable and broadband metamaterial absorbers (MAs) in details.

http://dx.doi.org/10.5772/67198

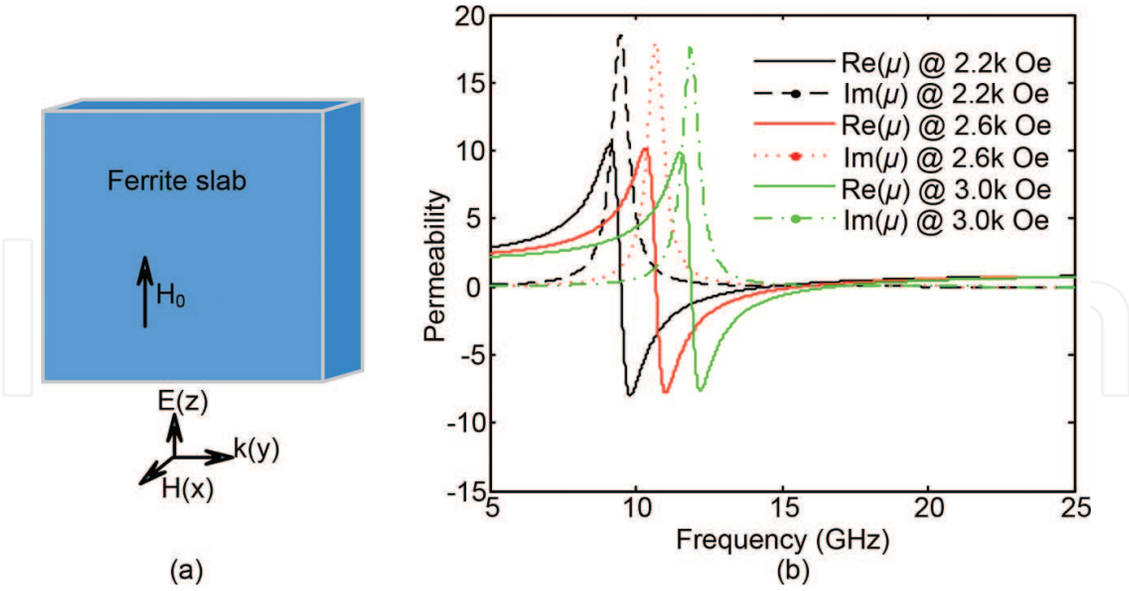

Figure 6. (a) A sample presentation of the ferrite under a DC magnetic bias, and (b) theoretical effective permeability of ferrite slab under different DC magnetic biases [41].

3. Numerical demonstrations for ferrite-based tunable metamaterials

3.1. Tunable dual-band configurations

The tunable dual-band metamaterial composed of ferrite slabs and SRR-wires is numerically discussed first. The schematic view of such structure with unit cell dimension of 2 mm is designed and shown in **Figure 7(a)**. As can be seen, the SRR and wire are placed in a 0.6-mm Rogers RT/duroid 5880 (ε_r = 2.2, tan δ = 0.0009) substrate and separated by 0.25 mm, and then two 0.7-mm TT1-3000 ferrite slabs are placed on the two sides of such substrate. In simulations, the structure is excited by a TEM wave with propagation vector (k) along the y-axis, and electric field vector (E) along the z-axis, as shown in **Figure 7(a)**. A DC magnetic bias acts on the ferrite slabs along the z-axis to excite the negative permeability property.

First, the single-band SRR-wires metamaterial and ferrites-wires metamaterial are demonstrated, respectively, to show the negative operating bands. The dimensional values of the two single-band metamaterials are optimized. For the SRR-wires structure, we have w_1 = 0.4 mm, d_1 = 1.6 mm, d_2 = 1.2 mm, w_2 = 0.1 mm, and w_3 = 0.3 mm. In this structure, a fictitious media (ε_r = 12.9, tan δ = 0.0005) is used to compare the ferrite media. The results shown in **Figure 7(b-i)** indicate that the single-band SRR-wires metamaterial has a negative operating band centered at 14.1 GHz. The transmission peak is −0.44 dB at 13 GHz. For the ferrite-wire structure, the fictitious media is replaced by ferrite media and the SRR is deleted. A 2-kOe magnetic bias acts on the ferrite slabs along the z-axis. The results shown in **Figure 7(b-ii)** indicate that the single-band ferrite-wire metamaterial has a negative operating band centered at 8.5 GHz. The transmission peak is −6.6 dB at 8.2 GHz.

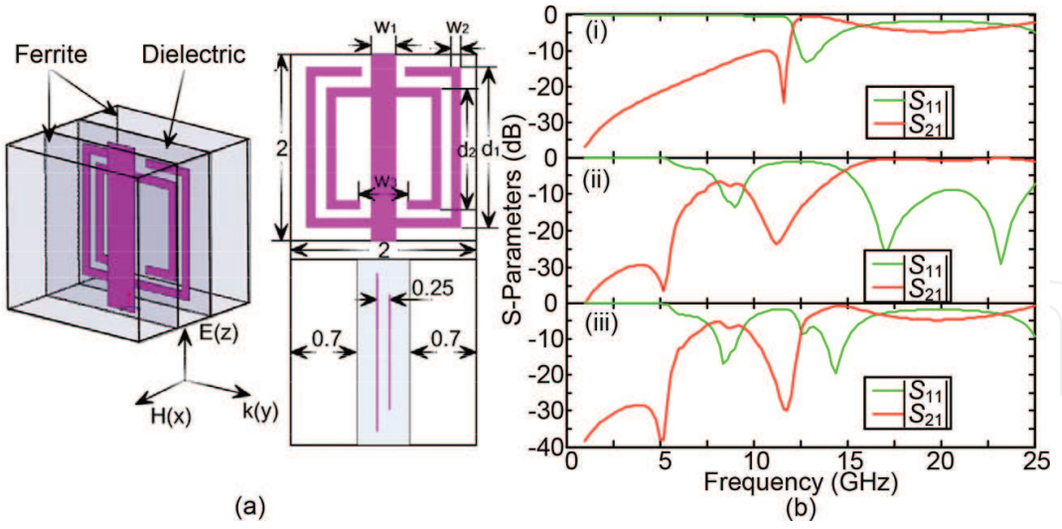

Figure 7. (a) The schematic of dual-band metamaterial composed of ferrite slabs and SRR-wires structure and (b) simulated transmission and reflection characteristics for the discussed configurations [41].

Then the combined dual-band metamaterial is investigated numerically. When the applied DC magnetic bias is set as 2 kOe, as shown in **Figure 7(b-iii)**, it clearly shows that there are two passbands centered at 8.4 and 15.3 GHz, respectively. The two transmission peaks are −5.6 and −1 dB at 8 and 14.6 GHz. Comparing the two single-band metamaterials and the dual-band metamaterial, the first passband contributed by ferrite slabs is not changed, while the second passband contributed by SRR in the combined dual-band metamaterial has a few blueshift. This is because that the positive part of the effective permeability is less than 1, as shown in **Figure 6**, so the resonance frequency of the SRR within the ferrite media is larger than the condition in the dielectric fictitious media.

To demonstrate the dual negative refractive index properties, the effective impedance and refractive index are obtained from the simulated S-parameters by using the retrieval method [46], and shown in **Figure 8(a)**. In **Figure 8(a)**, we see that the EM waves can be transmitted in the metamaterial in the above-mentioned two passbands. The real part of effective refractive index is below zero in such two passbands with very low loss due to the small imaginary part of effective refractive index.

To show the tunable property of the ferrite-based dual-band metamaterial, the transmission characteristics of such structure at different DC magnetic biases ranging from 2.2 to 3 kOe are numerically investigated and shown in **Figure 8(b)**. It can be seen that both the passbands are shifted accordingly. Specifically, the first passband is shifted from 8.5 to 10 GHz with tuning rate of about 1.875 MHz/Oe and the second passband is shifted from 14.6 to 15.8 GHz with tuning rate of about 1.5 MHz/Oe. The transmission peaks and bandwidths for the first operating band are not changed and the second operating band is narrowed when increasing the magnetic bias. As shown in **Figure 6**, this is because when increasing the magnetic bias, the negative permeability near the magnetic resonance is shifted rapidly; however, the positive permeability of the upper negative region is shifted slowly. Therefore, the resonance frequency of SRR within the ferrite media is shifted slowly.

http://dx.doi.org/10.5772/67198

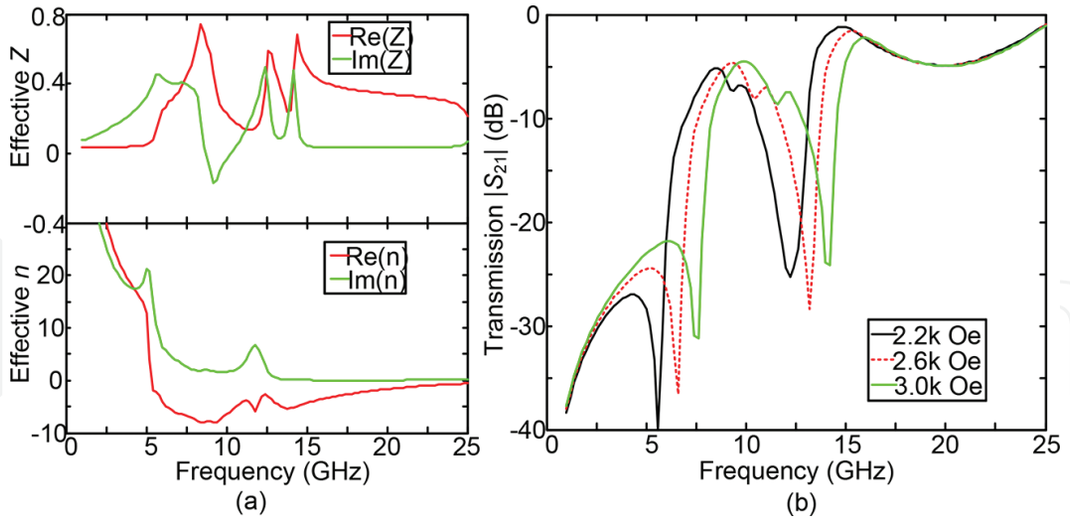

Figure 8. (a) Retrieved effective impedance and refraction, and (b) simulated tunability of the ferrite-based SRR-wire metamaterial [41].

Then the second kind of ferrite-based tunable dual-band metamaterial is discussed. We add the ferrite slabs to the Ω-like resonator [45] to achieve dual-band property. As shown in **Figure 9(a)**, the Ω-like resonators are placed in a 0.6-mm Rogers RT/duroid 6010 ($\varepsilon_r = 10.2$, $\tan\delta = 0.0023$) substrate and separated by 0.25 mm, and then two 0.7-mm TT1-3000 ferrite slabs are placed at the two sides of the substrate. The dimension of this dual-band metamaterial unit is 2 × 2 × 3 mm^3. The other structural values are optimized numerically: $w_1 = 0.4$ mm, $r = 1.6$ mm, and $w_2 = 0.2$ mm.

As shown in **Figure 9(b)**, the results indicate that the single-band Ω-like metamaterial has a negative operating band centered at 12.1 GHz, and the transmission peak is −0.2 dB at 12.6 GHz. The ferrite-based metamaterial under a magnetic bias of 2 kOe has two passbands, centered at 7 and 13.9 GHz, respectively. The transmission peaks are −6 and −1.6 dB at 8 and 13.5 GHz, accordingly. Also, the second passband contributed by Ω-like resonators in the combined dual-band metamaterial is larger than the condition in the single-band Ω-like metamaterial.

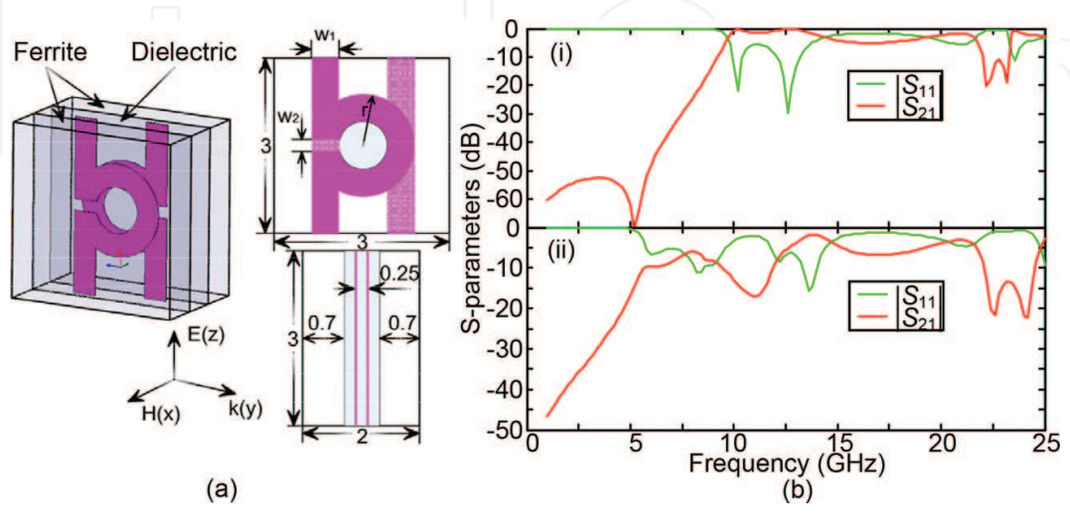

Figure 9. (a) The schematic of dual-band metamaterial composed of ferrites and Ω-like resonators, and (b) simulated transmission and reflection characteristics of the Ω-like metamaterial alone and loaded with ferrite [41].

The retrieved effective impedance and refractive index of such dual-band metamaterial, shown in **Figure 10(a)**, indicate that the EM waves can be transmitted in such metamaterial in the above-mentioned two passbands. The transmission properties of the structure are further simulated in different magnetic biases ranging from 2.2 to 3 kOe and shown in **Figure 10(b)**. It is seen that the two operating bands are shifted as well. Specifically, the first passband is shifted from 8.4 to 9.8 GHz with tuning rate of about 1.75 MHz/Oe, and the second passband is shifted from 13.7 to 15.3 GHz with tuning rate of about 2 MHz/Oe.

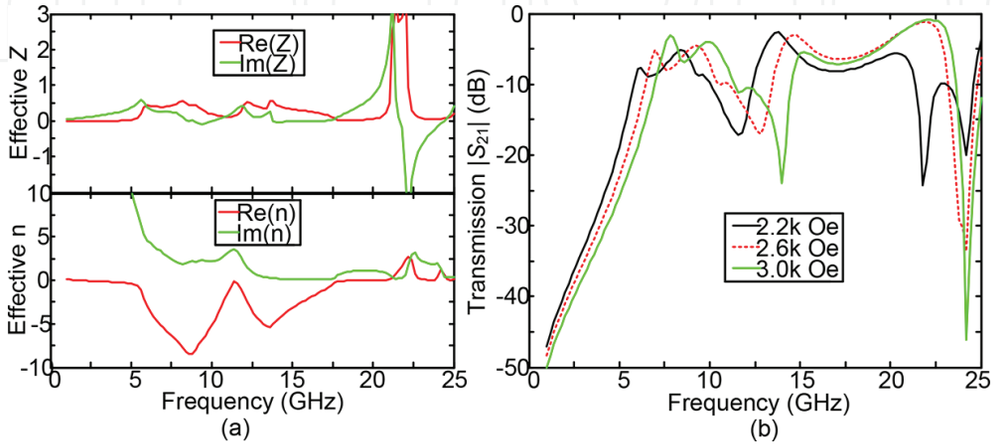

Figure 10. (a) Obtain effective impedance and refraction, and (b) numerical demonstrated tunability for the ferrite-based Ω-like metamaterial [41].

We now discuss the last kind of tunable dual-band metamaterial composed of ferrites and short wire pairs. As presented in **Figure 11(a)**, the short wire pairs are placed on a 0.25-mm Rogers RT/duroid 6010 substrate. Two TT1-3000 ferrite slabs are placed on the two sides of the substrate with air gaps, and then two other ferrite slabs are put on the other side of the substrate. The dimension of this dual-band metamaterial unit is 3 × 2 × 4 mm^3. The other structure values are optimized numerically: w_1 = 0.2 mm, w_2 = 0.4 mm, d = 3.4 mm, and w_3 = 0.6 mm.

As shown in **Figure 11(b)**, the results indicate that the single-band metamaterial has a negative passband centered at 16.5 GHz. The transmission peak is −0.2 dB at 15.9 GHz. The ferrite-based dual-band metamaterial under a magnetic bias of 2 kOe has two passbands centered at 7.9 and 16.5 GHz, respectively. The two transmission peaks are −7.3 and −0.5 dB at 8 and 16.2 GHz, respectively. The second passband contributed by short wire pairs in the combined dual-band metamaterial is larger than the condition in the single-band short wire pairs metamaterial.

As shown in **Figure 12(a)**, the retrieved effective impedance and refractive index of such metamaterial indicate that the EM waves can be transmitted in the metamaterial in the above-mentioned two passbands. The transmission properties of the dual-band metamaterial are further simulated in different magnetic biases ranging from 2.2 to 3 kOe, and are shown in **Figure 12(b)**. It can be seen that such two operating bands are shifted as well. Specifically, the first passband is shifted from 8.5 to 10.7 GHz with tuning rate of about 2.75 MHz/Oe. However, the second passband is shifted slightly, from 16.2 to 16.5 GHz with tuning rate of about 0.375 MHz/Oe. The second passband is narrowed when increasing the magnetic bias.

http://dx.doi.org/10.5772/67198

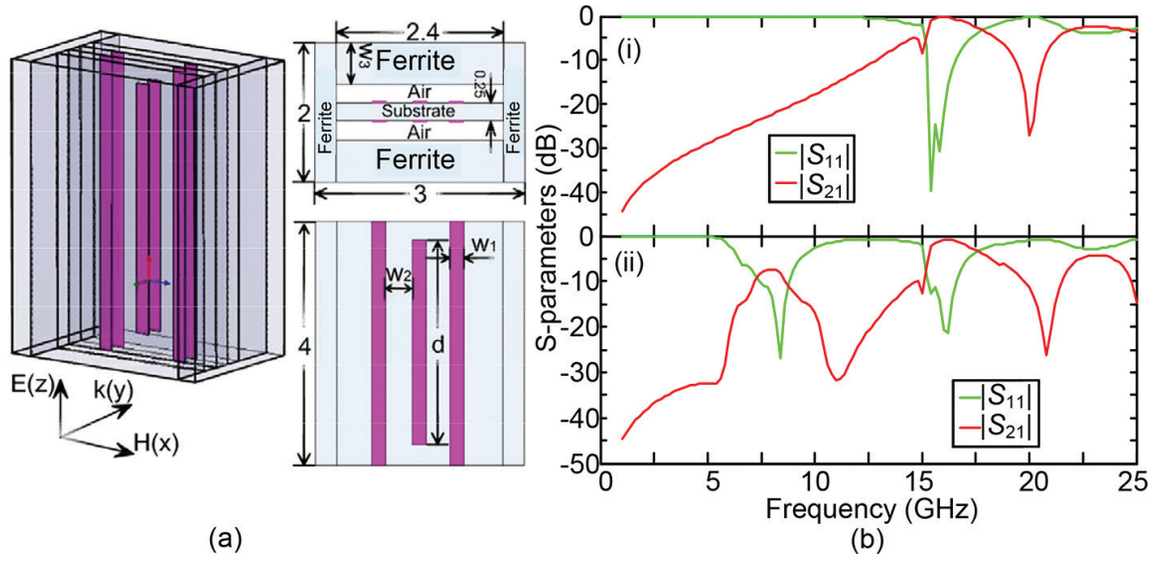

Figure 11. (a) The schematic of dual-band metamaterial composed of ferrites and short wire pairs, and (b) simulated transmission and reflection characteristics for the single-band short wire pair metamaterial and combined dual-band ferrite-based short wire pair metamaterial [41].

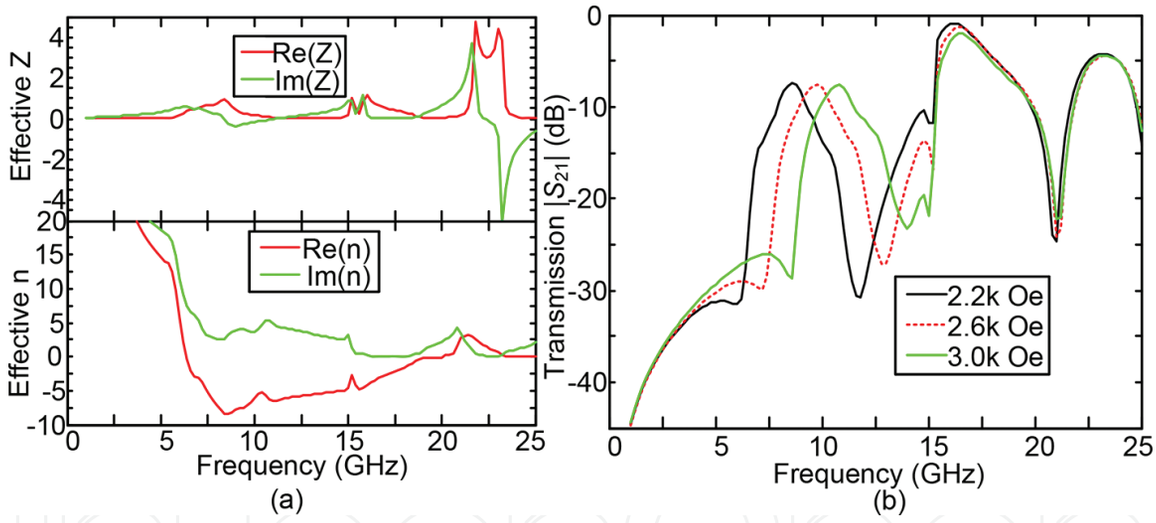

Figure 12. (a) Obtained effective impedance and refraction, and (b) the numerically demonstrated tunability for the ferrite-based short wire pair metamaterial [41].

From the above theoretical analysis and numerical investigations, the three dual-band metamaterials with different structures exhibit the same transmission characteristics and negative refraction. The two passbands of all the three metamaterials can be shifted arbitrarily and reversibly by easily changing the magnetic bias. Therefore, we can conclude that embedding the ferrites in the conventional resonance structure can fabricate the dual-band and tunable metamaterials.

3.2. Tunable triple-band configuration

The tunable triple-band negative permeability metamaterial is proposed by merging the ferrite slabs into the previously published dual-band negative permeability metamaterial based

on single-loop resonator (SLR) [47]. The SLRs provide two separate magnetic resonances, and the ferrite slabs under an applied DC magnetic bias exhibit the third magnetic resonance. All the three magnetic resonances can be controlled by adjusting the intensity of the magnetic bias.

The unit cell of the proposed tunable triple-band metamaterial is shown in **Figure 13(a)** [48]. A 0.03-mm-thick copper SLR is printed on one side of a Rogers TMM 4 substrate (ε_r = 4.5, loss tangent tan δ = 0.002). A commercial ferrite slab (G-4256 series, Trans-Tech Ltd.), with saturation magnetization $4\pi Ms$ = 1600 Gs, resonant beamwidth ΔH = 84 Oe, ε_r = 15.1, and loss tangent tan δ = 0.0002 is deposited on the other side of the TMM 4 substrate. As mentioned in Refs. [31, 32], the ferrite would damage the resonances of the metallic resonators if these two elements are directly touched. Therefore, a dielectric substrate should be inserted between the ferrite and the SLR structure (as shown in **Figure 13a**) to decouple this strong interaction.

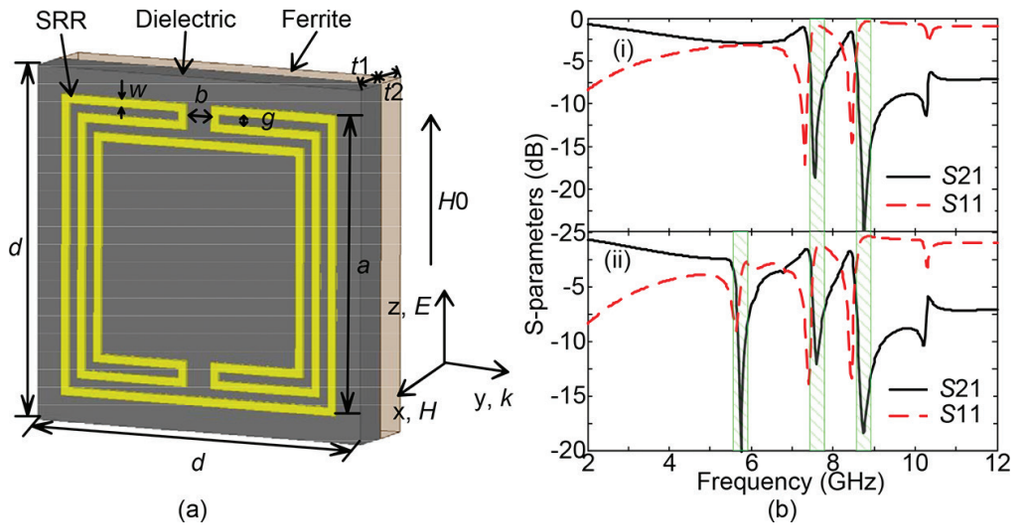

Figure 13. (a) Schematic representation of the tunable triple-band metamaterial unit cell and (b) numerical results of the transmission/reflection of the dual-band SLR structure metamaterial and the triple-band metamaterial [48].

In our simulations, the unit cell of the proposed ferrite-based metamaterial is placed in the center of a waveguide (with cross section of 4 mm × 4 mm) with perfect electric boundaries along the *z*-axis and perfect magnetic boundaries along the *x*-axis. The applied DC magnetic bias H_0 is set on the ferrite slab along the *z*-axis and the two wave ports placed in the front and back of the metamaterial along the *y*-axis. The geometric parameters of the metamaterial, obtained by numerical optimization, are shown as follows: a = 3.4 mm, b = 0.3 mm, d = 4 mm, $g = w$ = 0.1 mm, and $t_1 = t_2$ = 0.5 mm.

The transmission and reflections of the SLR array with and without ferrite under the DC magnetic bias of 1.4 kOe are computed, and the results are shown in **Figure 13(b)**. In order to make a fair comparison, in the case without ferrite slab, a same sized fictitious medium which has the relative dielectric constant of 15.1 and a loss tangent of 0.0002 is used. **Figure 13(b-i)** shows the case for dual-band SLR structure. There are three transmission deeps appearing at 7.5, 8.7, and 10.2 GHz, respectively. The first two transmission deeps

correspond to the magnetic resonances and the last one corresponds to the electric resonance, which have been numerically demonstrated in [47]. As shown in **Figure 13(b-ii)**, when a ferrite slab is merged, four transmission deeps appear at 5.7, 7.6, 8.7, and 10.2 GHz, respectively. Intuitively, the lowest deep results from the ferrite slab and the other three deeps come from the SLR structure. As we can see, the presence of ferrite has little influence on the three transmission deeps of the SLRs (only very slight frequency shifts), and the resonant frequency of the ferrite slab in simulation also agrees well with the theoretical result in **Figure 6**.

For better understanding the resonant behaviors of the ferrite-based metamaterial, in **Figure 14** we investigate the surface current distribution on the metallic SLR at each resonant frequency. It is clearly found that for the first transmission deep at 5.7 GHz, almost no surface currents are observed and so we can conclude that this resonance is contributed by the ferrite slab. For the other three transmission deeps—at 7.6, 8.7, and 10.2 GHz—the characteristics of surface currents are similar to that analyzed in [47].

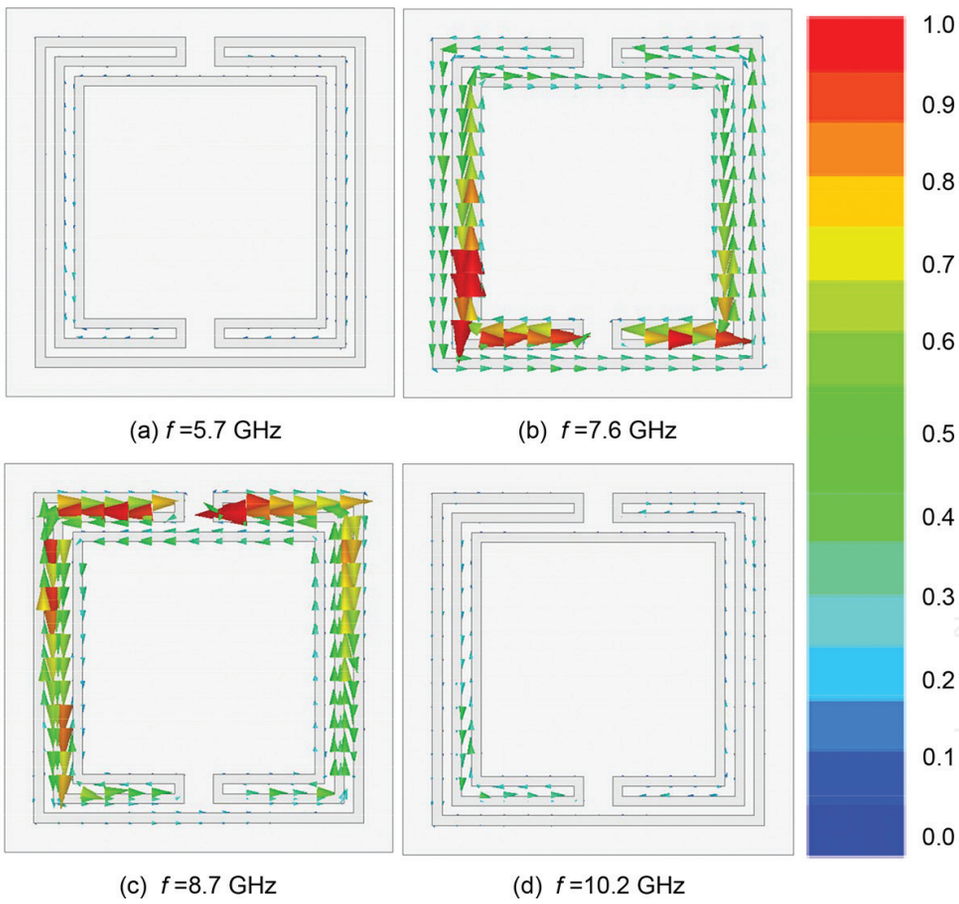

Figure 14. The simulated surface current distributions of the SLR structure at four resonant frequencies: (a) 5.7 GHz, (b) 7.6 GHz, (c) 8.7 GHz, and (d) 10.2 GHz. All the subplots use the same scale as shown in the right [48].

The effective constitutive parameters of the ferrite-based metamaterial are further determined from the numerically computed S-parameters by using the retrieval method [46]. As shown in **Figure 15**, the effective permeability curve exhibits three negative magnetic resonances

around 5.7, 7.5, and 8.5 GHz, where three μ-negative bands are obtained in 5.7–5.9, 7.5–7.7, and 8.5–9.0 GHz, respectively. It is also shown that a weak electric resonance appears at 10.2 GHz, which is not strong enough to obtain a ε-negative band. Comparison of theoretical permeability of ferrite medium (**Figure 6**) and the numerically retrieved effective permeability of the ferrite slab (inset of **Figure 15b**) shows that the intrinsic resonant frequencies of the ferrite in these two conditions agree very well. However, the μ-negative band in the simulation is much narrower than that of the theoretical analysis, because the theoretical result corresponds to a bulk ferrite medium, while the numerical one corresponds to a finite ferrite slab. Through this comparison, we can conclude that the intrinsic resonant frequency of the ferrite slab is not affected significantly by the magnetic resonances of the metallic SLR structure.

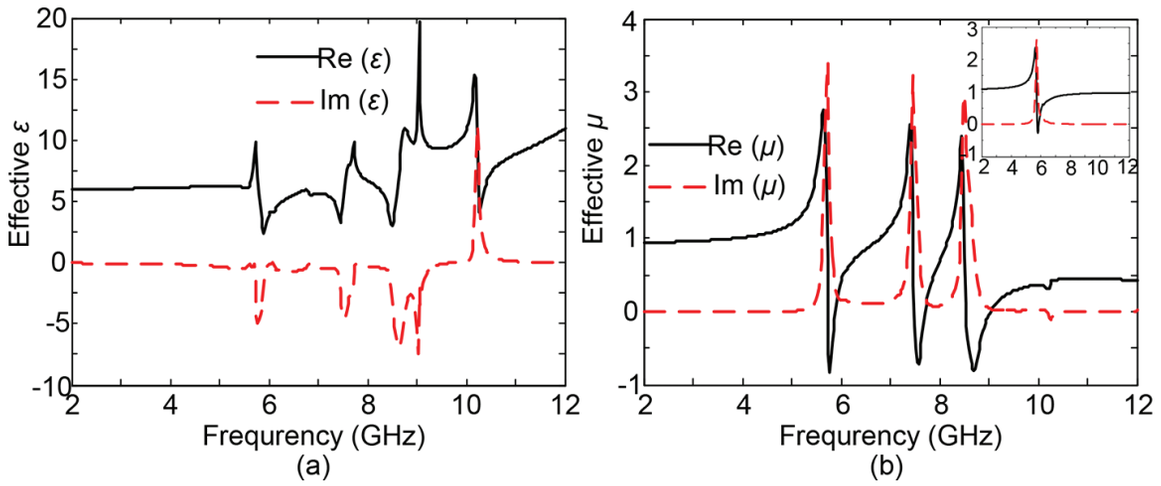

Figure 15. Retrieved effective media parameters: (a) effective permittivity and (b) effective permeability of the triple-band metamaterial. The inset figure in (b) corresponds to the retrieved permeability of the ferrite slab simulated at the same condition [48].

Now, let us investigate the tunability of this metamaterial under different DC magnetic biases. The tunable properties of transmissions as shown in **Figure 16(a)** indicate that increasing the DC magnetic bias from 1.2 to 1.6 kOe increases the first transmission deep sharply from 5.2 to 6.3 GHz; the second transmission deep increases very slowly; contrarily, the third transmission deep decreases from 8.8 to 8.6 GHz, because adjusting the DC magnetic bias in a small range cannot lead to an obvious shift of the second resonance which is very closely above the resonance of the ferrite slab. The third resonance decreases when increasing the DC magnetic bias in a small range because the theoretical $|\mathrm{Re}(\mu_{\mathrm{eff}})|$ of the ferrite slab changes to bigger values as shown in **Figure 6**.

The effective permeability curves under different DC magnetic biases are also determined from the simulated S-parameters, and the results are shown in **Figure 16(b)**. It is found that when increasing the DC magnetic bias, the first resonance increases sharply; the second resonance increases very slowly; and contrarily, the third resonance decreases. In all the cases under different DC magnetic biases, three μ-negative bands are obtained. We have also numerically found that when further increasing the intensity of the DC magnetic bias, first the frequencies of all the three resonances increase, then the resonance of the ferrite slab will

overlap with the two resonances of the SLR, and lastly the resonance of the ferrite slab will be above the two resonances of the SLR.

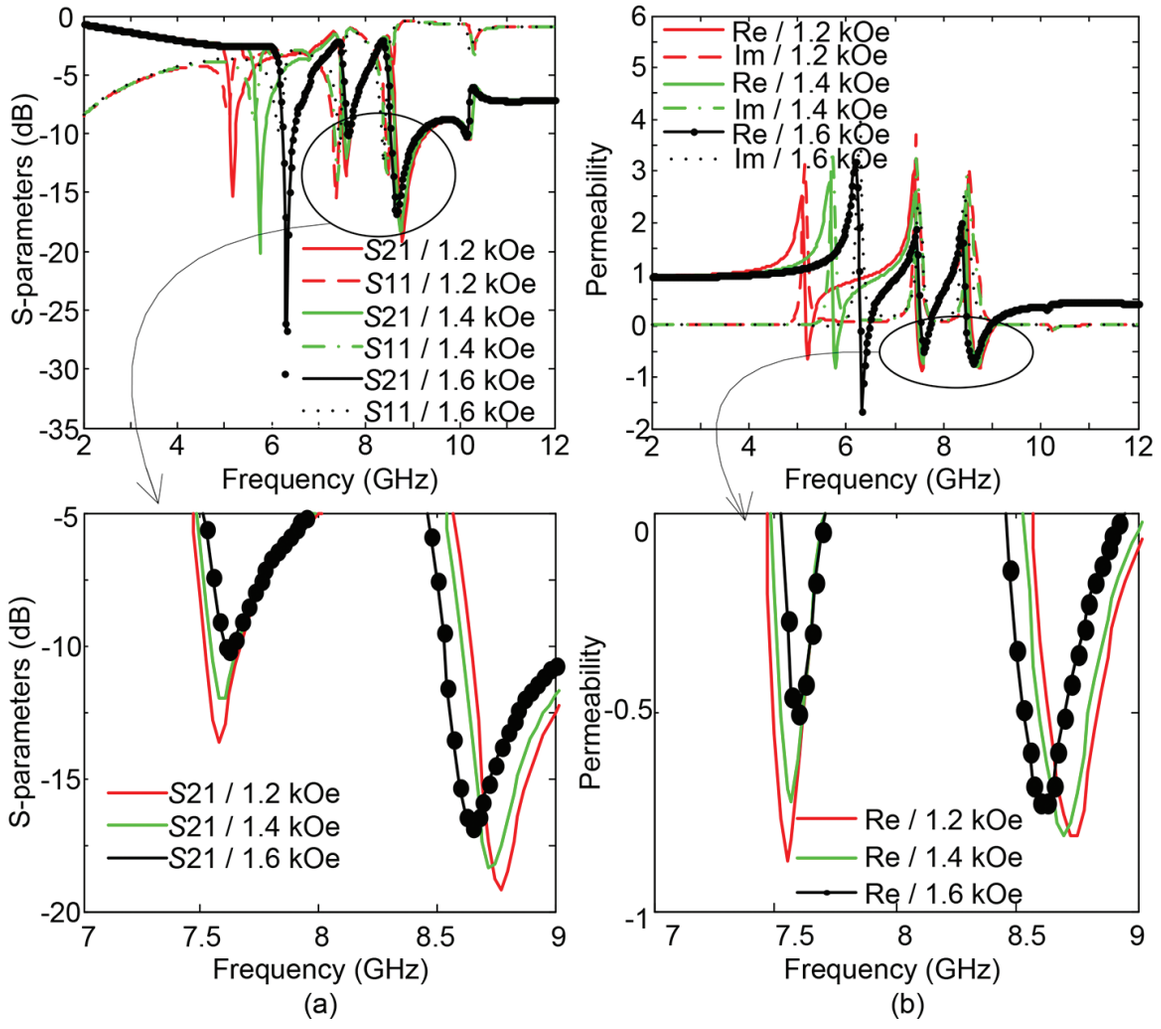

Figure 16. (a) Simulated transmissions and (b) retrieved effective permeability of the triple-band metamaterial under different dc magnetic biases ranging from 1.2 to 1.6 kOe [48].

3.3. Tunable THz ferrite-based metamaterial

Now we discuss the tunable THz ferrite-based metamaterial by using the well-developed ferrite film and metallic films technique [49]. Special ferrite films [such as the Lu Bi Fe O (LuBiIG) garnet film (see **Figure 17a**) [50] prepared by liquid phase epitaxy (LPE) method on a gadolinium gallium garnet (GGG) substrate] are used to achieve negative permeability. For the ferrite film used (saturation magnetization $4\pi Ms$ = 1750 Gs, resonant beamwidth ΔH = 1 Oe, ε_r = 3), the negative permeability band with very low magnetic loss can be obtained at the THz region. The silver films deposited on polyimide (Kapton 500HN, Krempel, Vaihingen/Enz, Germany) substrates using inkjet printing techniques (see **Figure 17b**) [51] are utilized to achieve negative permittivity. The substrate polyimide, with a relative permittivity of ε_r = 2.2, and loss tangent of tan δ = 0.0002, decouples the interactions between the ferrite films and the silver films.

Figure 17(c) shows the schematic view of the LuBiIG–silver–LuBiIG tunable metamaterial. The silver strip is deposited first on one of the two polyimide substrates, and such two substrates are placed close to the two LuBiIG films. The TEM wave propagates along the *y*-direction with the electric field along the *z*-direction. The applied DC magnetic field acts on the LuBiIG film along the *z*-direction. **Figure 17(d)** shows the theoretically calculated effective permeability and it exhibits typical resonant characteristics as well. When the applied DC magnetic field is set as 50 kOe, the real part of effective permeability is below zero in the frequency range of 0.142–0.145 THz. The imaginary part is much smaller than the real part and it means very low magnetic loss and thus can be ignored. Noticeably, the resonant frequencies of the ferrite film increase from 0.1397 to 0.1453 THz as the magnetic bias increases from 49 to 51 kOe.

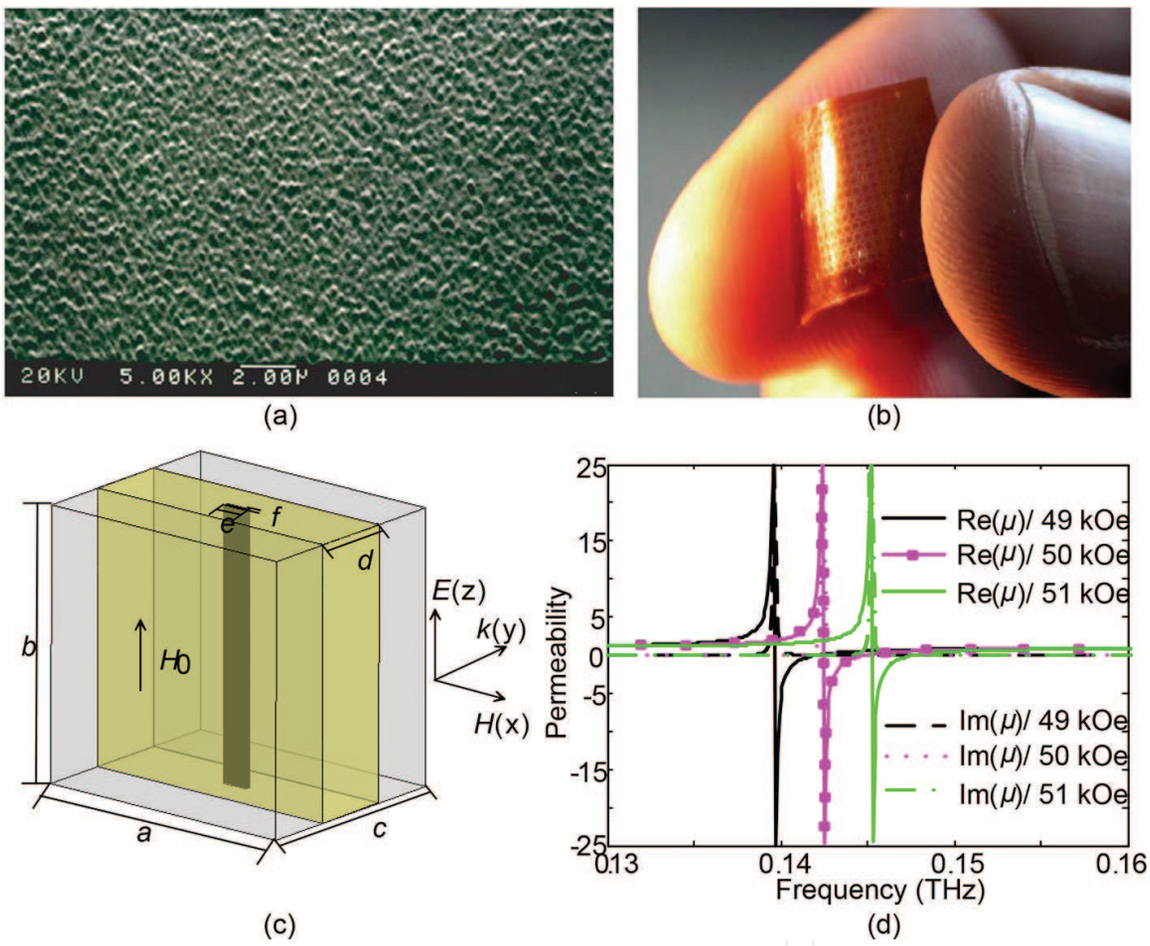

Figure 17. (a) Surface pattern images of the LuBiIG thin film [50], (b) photo of the silver SRR film [51], and (c and d) the tunable THz ferrite metamaterial unit and theoretical permeability of the ferrite film [49].

After the physical parameters of LuBiIG film, substrate, and silver are determined above, we now optimize the size of each film. The previous theoretical analysis results indicate that the effective permeability of LuBiIG film under 50 kOe is below zero in the frequency range of 0.142–0.145 THz, and the plasma frequency of silver strip array is about 1.5 THz when the periodicity *d* is about 100 μm. Based on these results, the optimized transmission results are depicted in **Figure 18**. The optimized parameters are found to be the following: *a* = 140 μm,

http://dx.doi.org/10.5772/67198

$b = c = 100$ μm, $d = 18.4$ μm, $e = 16$ μm, and $f = 2$ μm. From the simulation results as shown in **Figure 18**, the THz metamaterials have a passband centered at 0.1413 THz. The operating bandwidth (S21 > 8 dB) is about 2.4 GHz.

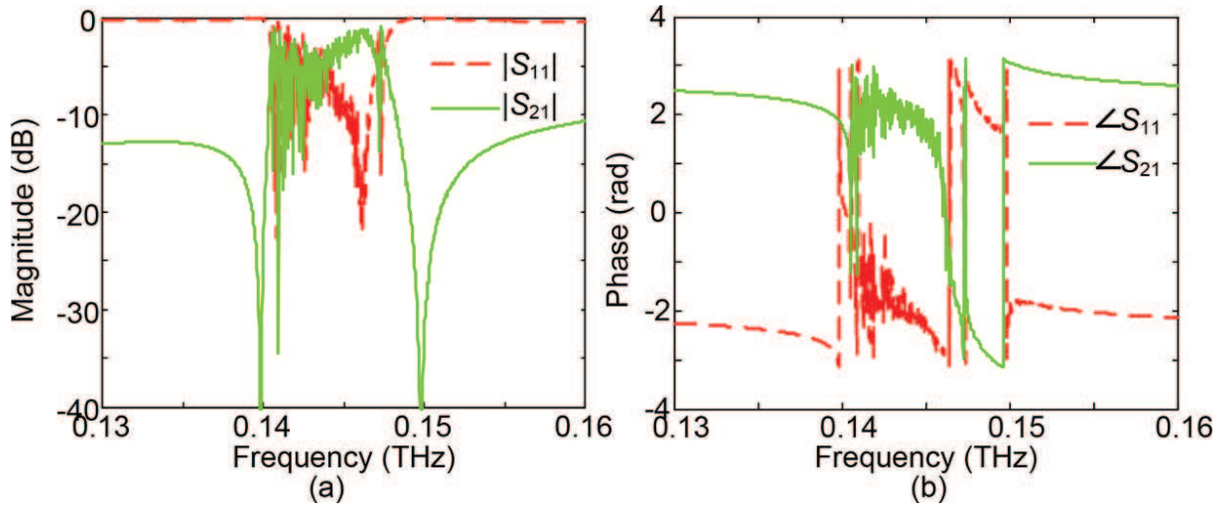

Figure 18. Simulated transmission and reflection characteristics LuBiIG–silver–LuBiIG structure metamaterials. (a) Magnitude. (b) Phase [49].

The effective refractive index values of the metamaterial are retrieved from the simulated parameters by using the retrieval method [46] and are shown in **Figure 19(a)**. It is seen that the metamaterial has negative refractive index in the range of 0.1401–0.1434 THz. Comparing the frequency bands of negative permeability (**Figure 17d**) and negative refractive index (**Figure 19a**) at same applied DC magnetic bias, a few frequency shifts appear because of the integrated dielectric substrate. Moreover, the real part of effective refractive index has a fixed value close to 10 at the frequency below 0.1401 THz and above 0.1434 THz.

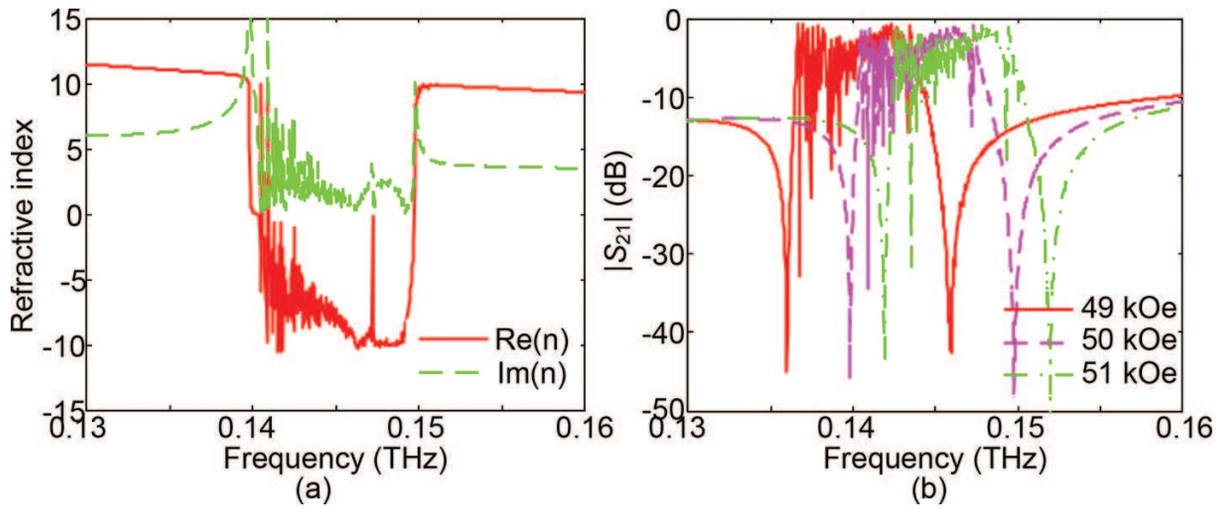

Figure 19. (a) Effective refractive index retrieved from S-parameters, and (b) tunability characteristics of metamaterials numerically demonstrated [49].

The tunability property is demonstrated earlier by tuning the applied DC magnetic field. As shown in **Figure 19(b)**, the transmission band shifts from 0.1385 to 0.1442 THz, when the applied DC magnetic bias is increased from 49 to 51 kOe. The tunability of such metamaterial depends on the tunability of the ferrite film. And the silver strip has a negative permittivity within a wide frequency region just below the plasma frequency. Therefore, the operating band of the proposed metamaterials can be tuned in a wide frequency band. Moreover, the shifted operating bandwidth and transmission peak do not vary strongly when the applied magnetic field is changed. This is mainly because of the fix saturation magnetization of the ferrite film.

4. Demonstrations for ferrite-based tunable metamaterial absorbers

Metamaterial absorbers (MAs) [52] have received most research attention due to the flexible design, subwavelength thickness, and high absorbing performance. MAs can be achieved at most of the frequency region by selecting the unit cell dimensions accordingly. The existence of such a huge operating spectral range enables the applications of MAs in various fields such as energy harvesting and thermal emitting and sensing [53–55]. Recently, various designs have been reported for MAs [56–60] and the corresponding numerical analysis and theory methods can be referred to, e.g., in [61–64].

However, the unique properties of MAs can be attributed to associated resonances, and thus MAs typically have narrow operating bandwidths. Researchers have proposed different methods to expand the operating bandwidths of MAs [65–69], while the flexible control of the MAs is still an intractable issue. Recent reports have shown that the absorbing frequencies of MAs can be dynamically adjusted by integrating tunable media (e.g., varactor diodes [70], liquid crystals [71], graphene [72], or phase-change materials [73]) to the traditional passive MAs. In some specific designs, researchers have advised to use oxide films [74] or film-coupled colloidal nanoantennas [75] as superstrate/substrate to adjust the absorbing frequencies. At the same time, we also designed a mechanic-tunable MA with moveable dielectric cover layer [76]. However, most of the reported designs have limited tuning range (e.g., [71–76]). Here we will first theoretically demonstrate that a properly geometrically configured ferrite-based metamaterial [77] has the ability to achieve high absorptivity with the added possibility to magnetically tune the absorption band, and then further demonstrate that by integrating a ferrite (the resonance bandwidth characteristic is not crucial any more) as the substrate or superstrate into a conventional planar MA, magnetic biased frequency-tunable absorption can also be achieved [78].

4.1. Tunable broadband metamaterial absorber based on ferrite and wire

The ferrite-wire MA unit cell is shown in **Figure 20(a)**. A 0.017-mm continuous copper wire is placed in the center of FR4 (ε_r = 4.4, tan δ = 0.02) substrate. Then two ferrite slabs (TT1-390, $4\pi M$s = 2150 Gs, ε_r = 12.7, ΔH = 648 Oe) are placed on the two sides of the FR4 substrate. The applied DC magnetic bias is applied on the ferrite slabs along the z-axis.

When an incident TEM wave propagates along the *y*-axis with electric field along the *z*-axis (shown in **Figure 20(a)**), the theoretical effective permeability of the ferrite slabs has been already analyzed as represented in Eq. (1).

The effective permeability of the ferrite slab used here under a magnetic bias of 3.2 kOe is calculated based on Eq. (1) and the results are shown in **Figure 20(b)**. It is seen that there is a magnetic resonance at 12 GHz and the real part of effective permeability is negative when frequency is larger than the magnetic resonance frequency. With the enlarged ΔH, the effective magnetic loss tangent $\tan \delta_\mu = \mathrm{Im}(\mu)/|\mathrm{Re}(\mu)|$ increases strongly in the negative permeability frequency band. Specifically, the $\tan \delta_\mu$ here has a value larger than 2.5 in the frequency region of 12.3–14.3 GHz. It indicates that the ferrite slabs can absorb most of the incident magnetic field component. Moreover, as shown in **Figure 20(c)**, the magnetic resonance of the ferrite slab can be shifted by adjusting the applied DC magnetic bias. When the magnetic bias increases from 2.6 to 3.4 kOe, the obtained magnetic resonance shifts from 10 to 12.5 GHz. And the big $\tan \delta_\mu$ is kept very well in the process of altering the applied DC magnetic bias.

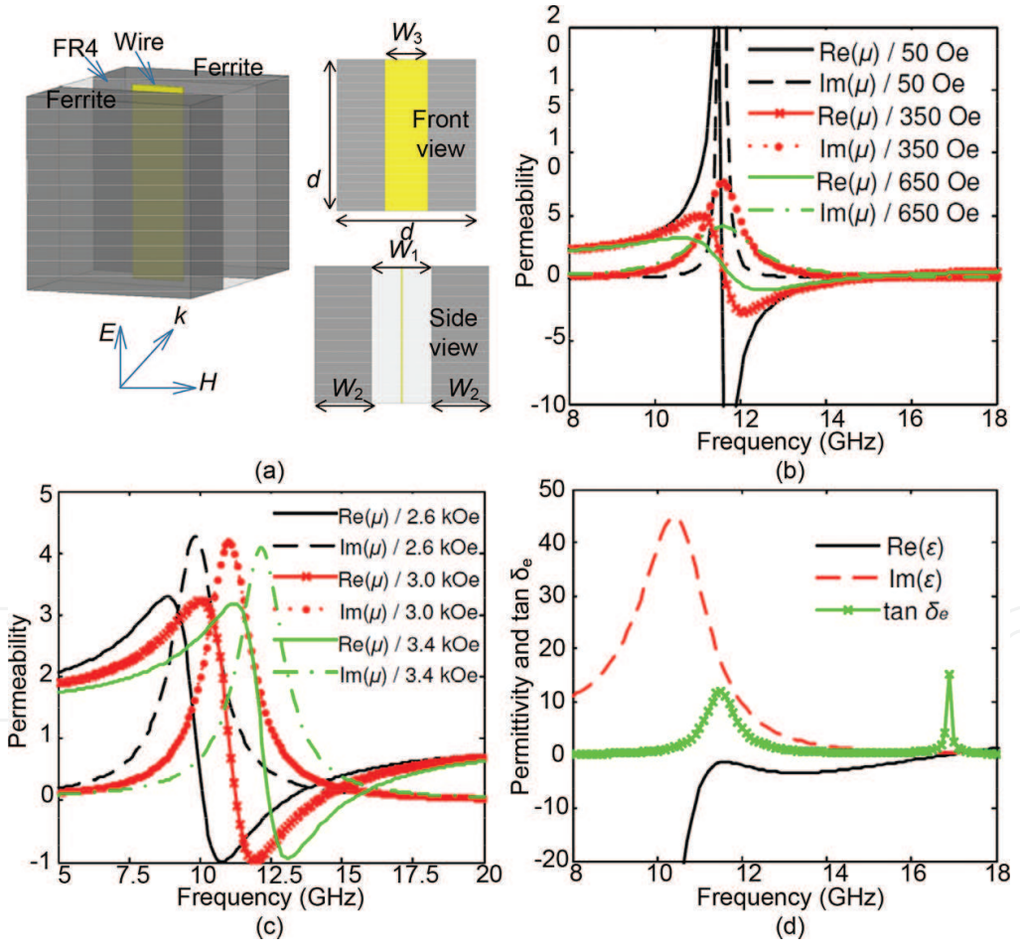

Figure 20. (a) Schematic diagram of the ferrite-wire MMA unit cell, (b) calculated theoretical effective permeability of the ferrite slabs with different resonance beamwidth ΔH and under a magnetic bias of 3.2 kOe, (c) calculated theoretical effective permeability of the ferrite slabs under different magnetic biases, and (d) calculated theoretical effective permittivity and effective dielectric loss tangent of the wire embedded in the ferrite slabs [77].

On the other hand, the effective permittivity of wires embedded in the ferrite slabs can be obtained as [31, 32]

$$\varepsilon_{\text{eff}} = \epsilon_f - \frac{\frac{\sigma_{\text{eff}}}{\omega}}{j + \left(\frac{\omega \mu_0 a^2 \sigma_{\text{eff}}}{2\pi}\right)\left[ln\frac{r_2}{r_1} + \frac{\mu_{\text{eff}}}{\mu_0}\left(ln\frac{a}{r_2} - 1.06\right)\right]} \tag{2}$$

where ε_f is the permittivity of the ferrite slab, σ_{eff} is the effective conductivity of the wire, r_1 and r_2 are the effective radii of the wire and the substrate layer, respectively, and a is the periodic lattice constant. As a result, the effective permittivity of wires can be calculated as shown in **Figure 20(d)**. It can be known that the real part of the effective permittivity is negative in a wide frequency region from DC to 17 GHz. And the effective dielectric loss tangent $\tan\delta_\varepsilon = \text{Im}(\varepsilon)/|\text{Re}(\varepsilon)|$ has a very large value ($\tan\delta_\varepsilon > 1$) in the range of 10–13 GHz, also shown in **Figure 20(d)**. Therefore, the continuous wires can absorb most of the incident electric field component. Lastly, we can expect that the ferrite-wire MA can absorb the incident EM waves with a very high absorptivity.

Next, based on the above theoretical analysis, we numerically discuss the absorption properties by optimizing the structural parameters to achieve the perfect impedance match and the highest absorption. As shown in **Figure 21(a)**, the powers of transmission $T(\omega)$, reflectance $R(\omega)$, and absorptivity $A(\omega) = 1 - T(\omega) - R(\omega)$ are presented respectively. The final structure parameters are obtained: $d = 2$ mm, $w_1 = 0.959$ mm, $w_2 = 0.909$ mm, and $w_3 = 0.585$ mm. It can be seen that both the transmission $T(\omega)$ and reflectance $R(\omega)$ have very small values in the X-band (8–12 GHz) and as a result the absorptivity $A(\omega)$ can achieve near-uniform value. Specifically, the smallest reflectance $R(\omega)$ is about 0 at 9.9 GHz. The peak absorptivity $A(\omega)$ is about 98.2% at 9.9 GHz, and the frequency band of $A(\omega)$ over 90% is about 2.3 GHz. It should be noted that the high performance absorbing frequency band in simulation is lower than the frequency band of theory. This is due to the fact that the theoretical results discussed previously are under ideal conditions [31, 32]. That means the theoretical expressions in this chapter only provide the design guidance, and the numerical optimizations are more accurate and useful for the proposed ferrite-based MA.

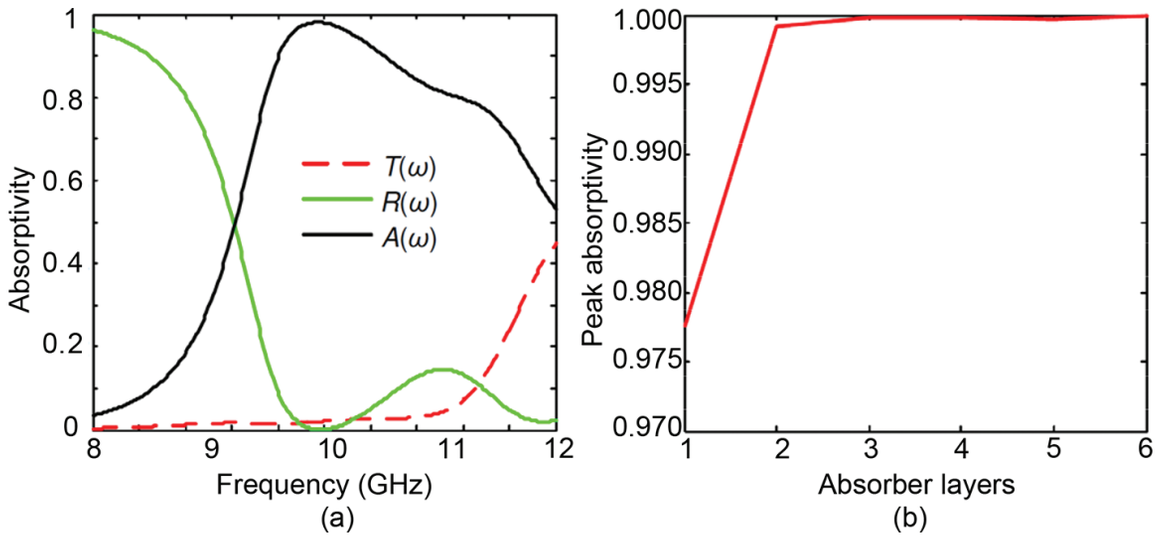

Figure 21. (a) Simulated transmission, reflectance and absorptivity characteristics of the ferrite-wire MMA under a magnetic bias of 3.2 kOe, and (b) absorptivity characteristic of ferrite-wire MA as a function of the number of layers [77].

Moreover, the absorptivity can be further enhanced by adding more layers. For instance, **Figure 21(b)** shows the absorptivity property as a function of the layers. As can be seen, $A(\omega)$ rises quickly with the increased layers and approaches asymptotically to 1. Two MA layer can achieve an absorptivity of about 99.92%. At this condition, the entire MA thickness is only $\lambda/5$ for the center operating frequency of 9.9 GHz.

In order to demonstrate the tunability of the operating frequency, **Figure 22(a)** shows the simulated shift property of the MA in different magnetic biases. As can be seen, the peak absorptivity and the bandwidth are not changed, the frequency of the peak absorptivity $A(\omega)$ shifts from 6.75 to 11.75 GHz as the applied DC magnetic bias changes from 2 to 4 kOe with a near-linear tuning rate of 2.625 MHz/Oe. We can further expect that the proposed ferrite-wire MA can operate at higher frequencies, such as terahertz region based on the discussed techniques [49].

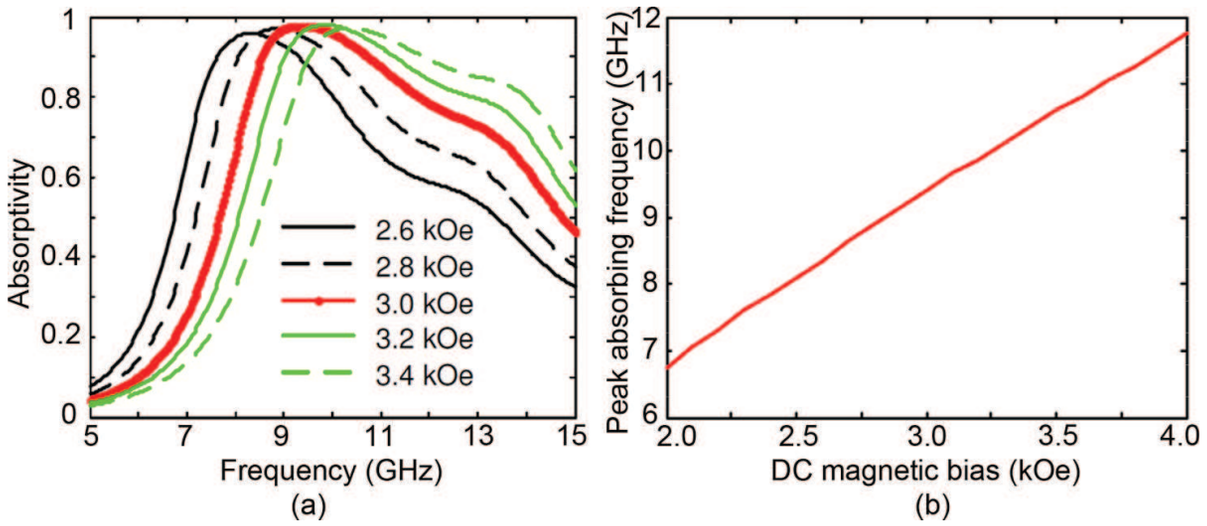

Figure 22. Peak shift properties of the absorptivity of the ferrite-wire MMA under different magnetic biases. (a) The absorption band characteristics under different magnetic biases, and (b) the frequency of the peak absorptivity as a function of the magnetic bias [77].

4.2. Tunable ferrite-based metamaterial absorbers

The new ferrite inspired MAs are schematically shown in **Figure 23(a)**. Similar to [76], we use the electric-LC (ELC) resonators with a metallic plate to achieve a conventional MA. The ELC array is printed on one side of the FR4 substrate and a full-sized metallic plate is covered on the other side of the FR4. For the purpose of achieving tunable property, we design two strategies by integrating ferrite into the passive MA. In the first case (MA1), the ferrite slab is inserted between the FR4 and ground plane [see the left plot of **Figure 23(b)**]. Both the ferrite and the FR4 layers service together as a substrate. In the second case (MA2), the ferrite layer is employed as a superstrate [see **Figure 23(b)**, right plot] and another FR4 layer is placed between the ferrite and the passive MA. The two MAs are analyzed and measured in an X-band rectangular waveguide closed measurement system as shown in **Figure 23(c)**.

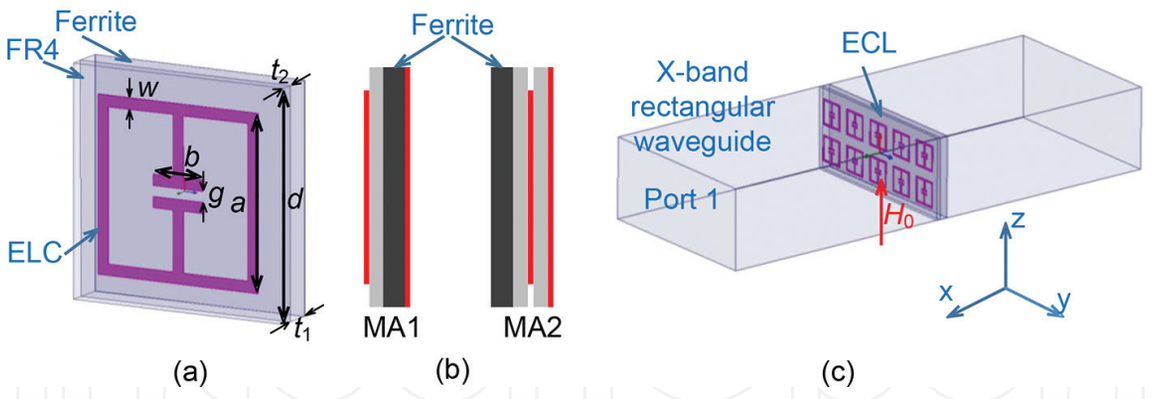

Figure 23. (a) Unit cell of the ferrite-based tunable MA, (b) side views of two MA models, and (c) schematic representation of measurements [78].

The relative permittivity of ferrite used in this chapter is 13.8 (loss tangent is 0.0002), and $4\pi Ms$ = 1830 Gs, ΔH = 22 Oe. As shown in **Figure 24**, when the applied DC magnetic bias increases from 1.1 to 1.9 kOe, the permeability of ferrite shows blueshift with shift rate of about 20 MHz/Oe. At the frequency band of interest (X-band), it can be seen that the effective permeability changes from positive to negative when the magnetic field increases. This changing feature can be used for dynamical tunability of the host media of ELC. Different from our previous work [77] where the ferrite's tunable permeability is employed for synthesizing magnetically controllable metamaterials, the frequency band we are interested in is outside the intrinsic resonant band of ferrite. Therefore, the required ferrite is not limited by its narrow resonant bandwidth and can be generally substituted by any other types of ferrites.

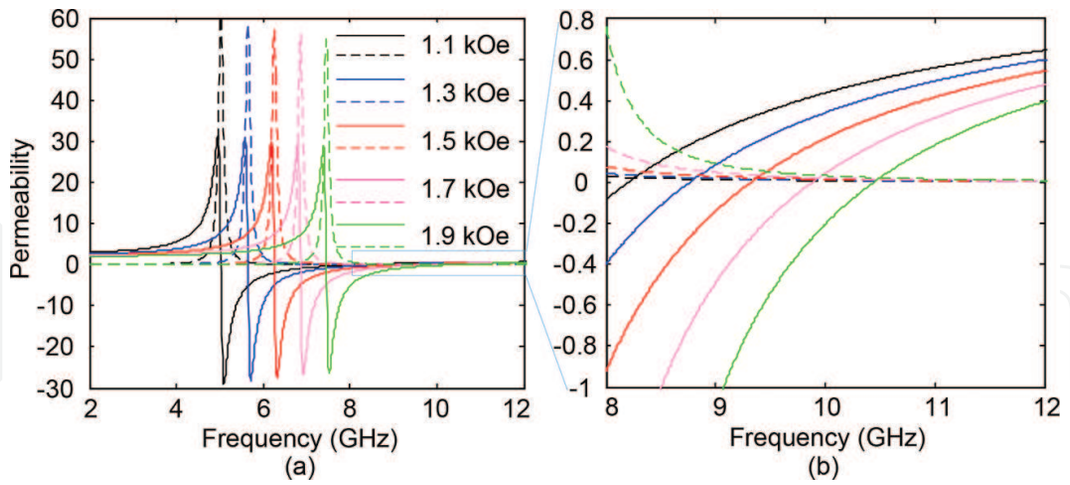

Figure 24. Permeability dispersion of the ferrite under different magnetic fields, where solid and dashed curves denote real and imagery parts, respectively. Zoomed plot shows the permeabilities of ferrite in the frequency range of interest (8–12 GHz) [78].

Now we optimize the ELC geometrical parameter by employing numerical simulations (CST). Due to the lab-experimental restriction, the thicknesses of the metallic patterns, FR4, and ferrite slab are fixed to be 0.034, 0.5, and 1 mm, respectively. The geometrical parameters for

http://dx.doi.org/10.5772/67198

MA1 are optimized to be a = 2.94 mm, b = 1 mm, $w = g$ = 0:2 mm, and d = 4.5 mm. For the case of MA2, the additional FR4 layer would result in the red-shift of the resonance outside of 8–12 GHz. To avoid this problem, it should slightly reduce the size of the ELC resonator to a = 2.82 mm. The applied DC magnetic bias is preset as 1.55 and 1.6 kOe in simulations for both structures. The two MA samples are fabricated and measured in an X-band rectangular waveguide measurement system by using Agilent N5230A vector network analyzer (VNA). Specifically, the FR4 with ELC resonators and ferrite slab are put into the waveguide sequentially for MA1; the ferrite slab, FR4, and passive MA are staked one over the other within MA2. For these two structures, a metallic plate tightly covers the waveguide port to prevent any energy leakage. A tunable z-directed DC magnetic field generator is applied on the MA samples. Finally, the rectangular waveguide filled with MA samples is connected to the coaxial cable of VNA by using a waveguide-to-coaxial converter.

As shown in **Figure 25(a)** and, **(b)** each MA indicates a clear near-uniform absorption peak. The measured peak frequencies are higher than the simulated ones slightly. This is because the ferrite slabs are difficult to be placed seamlessly to the FR4 inside the waveguide. However, it should be noticed that this does not affect the tunability property of the ferrite-based MAs.

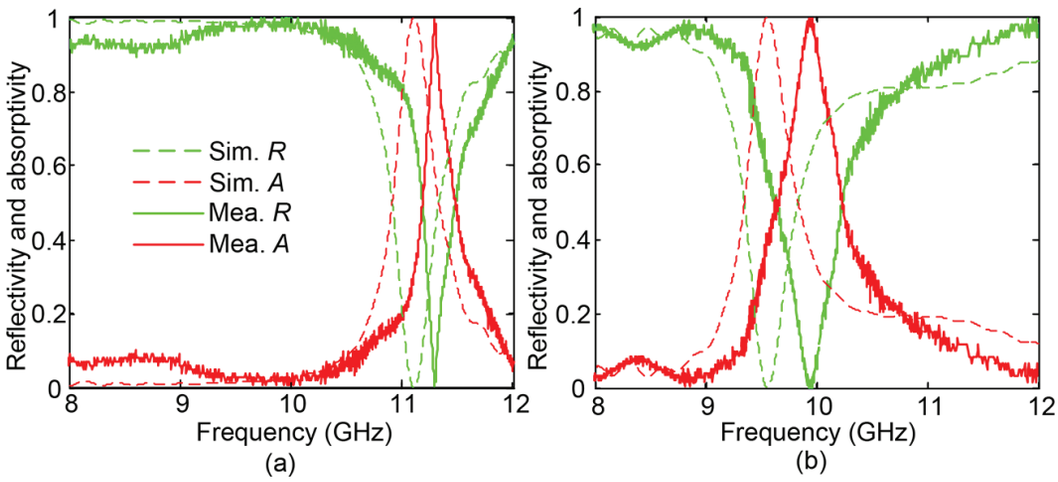

Figure 25. Simulated and measured reflectivity and absorptivity properties for the (a) MA1 and (b) MA2 [78].

The absorptivity of the MAs can be dynamically controlled by changing the applied magnetic bias. In **Figure 26**, it can be seen that when the magnetic field is increased gradually, the absorption peaks blueshift for both MAs. Particularly, see **Figure 26(a)** and **(b)**, an absorption peak appears at 10.75 GHz with peak absorptivity of 85.5% for MA1 free of magnetic field in simulation. When the magnetic field is gradually increased from 1.15 to 1.95 kOe, the absorbing frequency moves from 10.99 to 11.29 GHz in simulation (11.17 to 11.45 GHz in measurement). Meanwhile, the absorptivity increases from 97.8% to nearly 100% and then drops to 93.3% in simulation (increases from 85% to nearly 100% and then descends to 80% in measurement). Similar frequency shift and absorptivity change performance can be found in **Figure 4(c)** and **(d)** for MA2, as well. It is easy to conclude that the frequency shift rates of MA1 and MA2 are about 0.36 and 0.18 MHz/Oe, respectively.

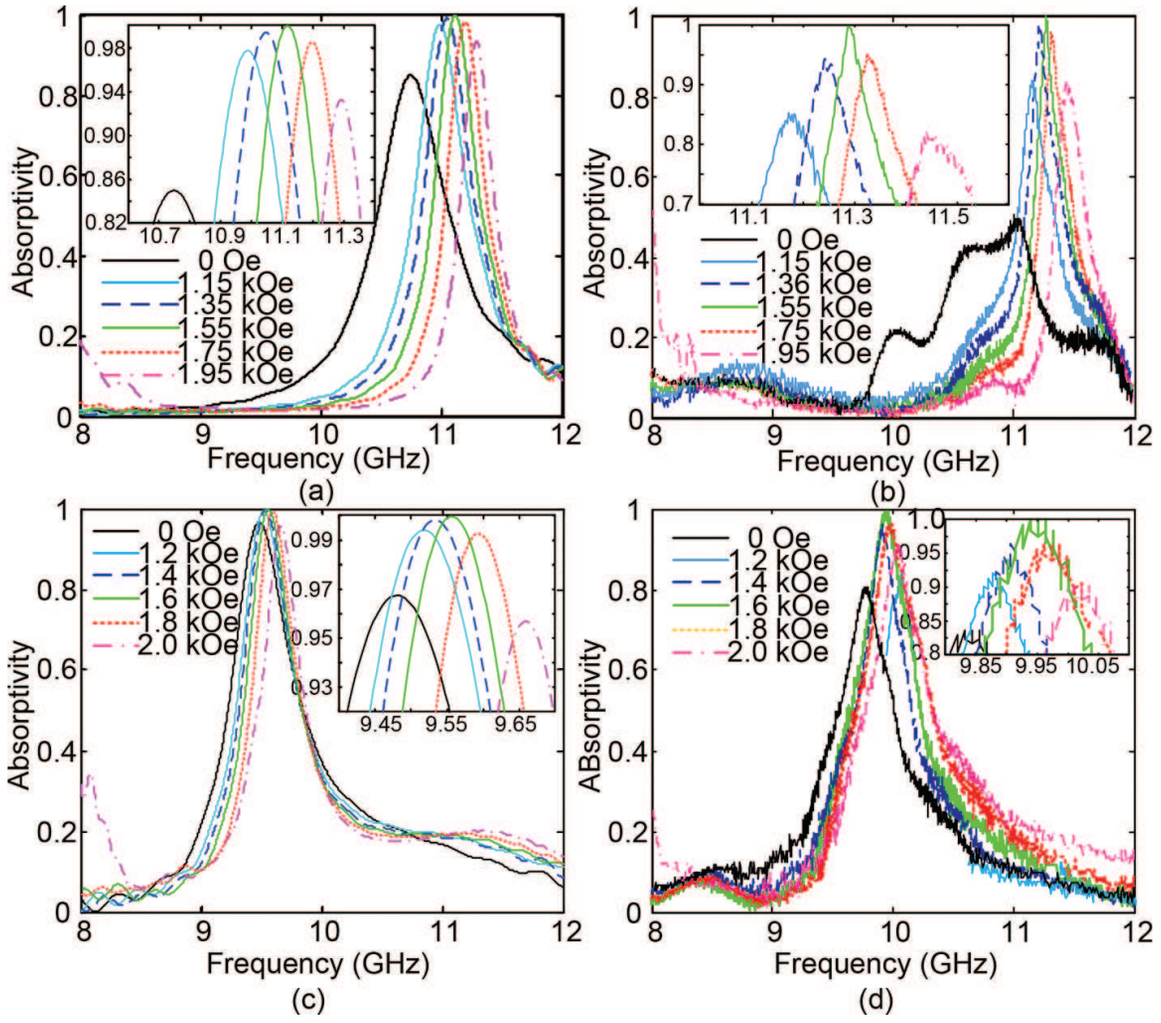

Figure 26. (a and c) Simulated and (b and d) measured absorptivity properties under different magnetic fields for MA1 and MA2, respectively. Insets show the zoom-in plots [78].

When closely looked at the measured results and the corresponding simulations at the same magnetic bias, the absorbing frequencies for both MAs have higher measured values compared with simulations. Moreover, compared to the two MA configurations, the shift rate of MA1 is larger than MA2. This is because the resonance-induced localized electromagnetic fields are mainly located in the substrates rather in the superstrates, and therefore the changing features of the MAs are more sensitive on the substrates.

In the above discussions, both thicknesses of the ferrite slab and the FR4 are fixed at 1 and 0.5 mm, respectively. Now we further discuss the effects of the thicknesses of the ferrite and the FR4 on the absorbing performances of the tunable MAs. For examples, we fix the thickness of one layer (either ferrite or FR4) and change the other layer to see the tunable absorptions of the two MAs. For MA1, the FR4 (ferrite) slab is fixed to be 0.5 mm (1 mm) and the ferrite (FR4) layer is changed from 0.6 to 1.4 mm (0.1 to 0.7 mm). The corresponding numerical results are concluded in **Figure 27(a)** and **(b)**. For MA2, the FR4 (ferrite) layer is fixed to be 0.5 mm (1 mm) and the ferrite (FR4) layer is tuned from 0.8 to 1.1 mm (0.3 to 0.6 mm), and the results

http://dx.doi.org/10.5772/67198

are shown at **Figure 27(c)** and **(d)**. For MA2, it should be noted that we only change one FR4 layer which acts as a superstrate and the FR4 substrate between the ELC and ground plane is kept unchanged.

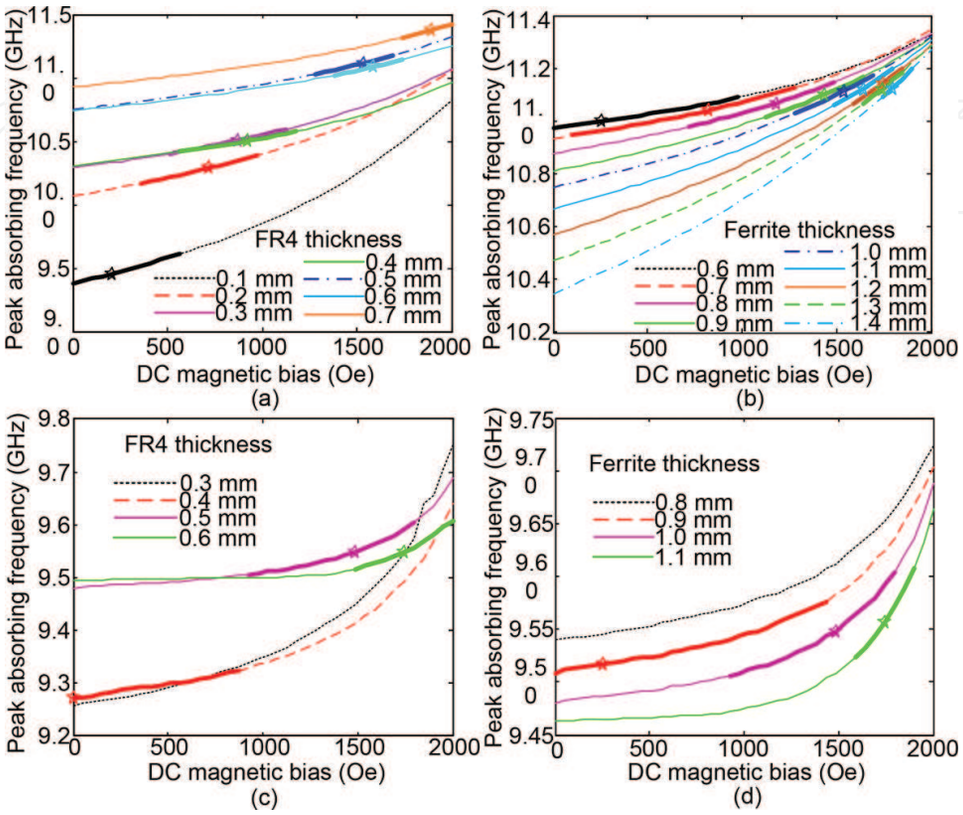

Figure 27. Simulated absorbing frequencies of MAs for MA1 when the thicknesses of (a) FR4 and (b) ferrite layers are changed, and for MA2 when the thicknesses of (c) FR4 and (d) ferrite layers are changed. The star and bold part at each curve correspond to the nearly uniform absorptivity and the band of absorptivity larger than 98.5%.

More specifically, when the magnetic field is increased, the resonant frequencies of the MAs blueshift. This is in accordance to the theoretical results shown in **Figure 24**. For a larger thickness of the FR4 or ferrite slab, a larger magnetic bias is required to ensure a nearly uniform absorptivity (represented as stars in **Figure 27**) and the magnetic field for a high absorptivity (>98.5%) is reduced (see the bold part of each curve). Fortunately, one can also increase the magnetic bias to reduce the effective permeability of the ferrite. The impedance matching can be regained at a certain magnetic field at that case. Moreover, the shift rate of the absorbing frequency is nearly linear when the magnetic field is weak, and becomes strongly nonlinear when the magnetic field increases, especially for the MA2 [see **Figure 27(c)** and **(d)**]. On the other hand, some unfavorable properties can also be obtained when the thickness of the FR4 or the ferrite slab is increased. Specifically, for thicker FR4, the initial peak absorptivity frequencies increase, and meanwhile the frequency shift rates decrease for both MAs. Contrarily, as shown in **Figure 27(b)** and **(d)**, inverse trends are found when the thicknesses of the ferrite layers are increased.

From previous discussions, we know that the resonant frequency of the MA becomes more sensitive to the magnetic field for thinner FR4, but the high absorptivity band is reduced as well. As a result, it is important to get an equilibrium such that the frequency shift range is relatively large and at the same time the MA has a uniform absorptivity in the tuning range. As an example, we choose FR4 between the ELC and ground plane to be 0.65-mm thick for MA2, and for the other FR4 to be 0.1-mm thick. For this condition, the ferrite slab is close enough to the ELC and so can give more contributions on the tunability, and at the same time, the other enlarged FR4 can offset the impedance mismatching between MA and background medium. In **Figure 28** we see that the resonant frequency of the MA can be shifted from 8.6 to 9.65 GHz and the absorptivity at each resonance can be kept higher than 98.5%, when the magnetic field increases from 0 to 1.9 kOe. The obtained shift range is as large as 11.5%. This is a very wide frequency tuning range (more than three times larger than those reported in previous works [71, 72, 74]).

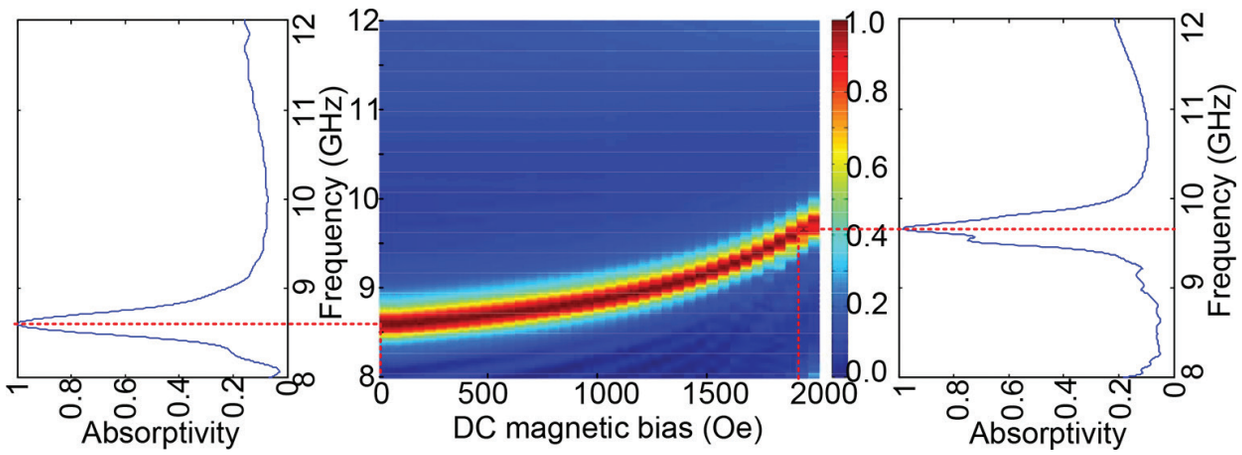

Figure 28. Simulated absorptivity of MA2 under different magnetic biases with optimized dimensional parameters. The middle plot presents the absorptivity spectra as a function of magnetic field and frequency. The left and right plots show the absorptivities at magnetic field of 0 and 1900 Oe, respectively [78].

5. Conclusions

In this chapter, we presented the recent achievements in our research group for the tunable metamaterials by using the ferrite as the substrate of metamaterials. We presented the designs and theories of single-, dual-, and triple-band tunable metamaterials based on the ferrite, and the design of metamaterial absorbers based on the ferrite. It indicates that the proposed tunable metamaterials have many advantages compared with other active and tunable metamaterials.

Acknowledgements

This work was supported by the National Natural Science Foundation of China (Grant No. 61371047, 61601093), and the Science and Technology Planning Project of Guangdong Province

and Sichuan Province of China (Grant No. 2016A010101036, 2016GZ0116, 2016GZ0061). Y. Huang also gratefully acknowledges the Scholarship Award for Excellent Doctoral Student granted by Ministry of Education of China (Grant No. A03003023901006).

Author details

Yongjun Huang*, Jian Li and Guangjun Wen

*Address all correspondence to: yongjunh@uestc.edu.cn

Centre for RFIC and System Technology, School of Communication and Information Engineering, University of Electronic Science and Technology of China, Chengdu, China

References

[1] N. Engheta and R. W. Ziolkowski. Metamaterials: Physics and Engineering Explorations. New Jersey: John Wiley & Sons; 2006.

[2] R. A. Shelby, D. R. Smith, and S. Schultz. Experimental verification of a negative index of refraction. Science. 2001;**292**:77–79.

[3] S. H. Lee, C. M. Park, Y. M. Seo, and C. K. Kim. Reversed Doppler effect in double negative metamaterials. Phys. Rev. B. 2010;**81**:241102(R).

[4] Z. Duan, C. Guo, and M. Chen. Enhanced reversed Cherenkov radiation in a waveguide with double-negative metamaterials. Opt. Express. 2011;**19**:13825–13830.

[5] T. J. Cui, X. Q. Lin, Q. Cheng, H. F. Ma, and X. M. Yang. Experiments on evanescent-wave amplification and transmission using metamaterial structures. Phys. Rev. B. 2006;**73**:245119.

[6] C. Argyropoulos, N. M. Estakhri, F. Monticone, and A. Al`u. Negative refraction, gain and nonlinear effects in hyperbolic metamaterial. Opt. Express. 2013;**21**:15037–15047.

[7] H. Y. Dong, J. Wang, K. H. Fung, and T. J. Cui. Super-resolution image transfer by a vortex-like metamaterial. Opt. Express. 2013;**21**:9407–9413.

[8] X. Zhang and Z. Liu. Superlenses to overcome the diffraction limit. Nat. Mater. 2008;**7**:435–441.

[9] D. Schurig, J. J. Mock, B. J. Justice, S. A. Cummer, J. B. Pendry, A. F. Starr, and D. R. Smith. Metamaterial electromagnetic cloak at microwave frequencies. Science. 2006;**314**:977–980.

[10] C. M. Watts, X. Liu, and W. J. Padilla. Metamaterial electromagnetic wave absorbers. Adv. Mater. 2012;**24**:OP98–OP120.

[11] R. Marqu´es, F. Mart´ın, and M. Sorolla. Metamaterials With Negative Parameters: Theory, Design and Microwave Applications. New Jersey: John Wiley & Sons; 2007.

[12] N. K. Grady, J. E. Heyes, D. R. Chowdhury, Y. Zeng, M. T. Reiten, A. K. Azad, A. J. Taylor, D. A. R. Dalvit, and H. T. Chen. Terahertz metamaterials for linear polarization conversion and anomalous refraction. Science. 2013;**340**:1304–1307.

[13] I. Gil, J. Bonache, J. García-García, et al. Tunable metamaterial transmission lines based on varactor-loaded split-ring resonators. IEEE Transactions on Microwave Theory and Techniques. 2006;**54**:2665-2674.

[14] A. Vélez, J. Bonache, and F. Martin. Varactor-loaded complementary split ring resonators (VLCSRR) and their application to tunable metamaterial transmission lines. IEEE Microwave Wireless Components Lett. 2008;**18**:28–30.

[15] D. Wang, L. Ran, H. Chen, et al. Active left-handed material collaborated with microwave varactors. Appl. Phys. Lett. 2007;**91**:164101.

[16] K. Aydin and E. Ozbay. Capacitor-loaded split ring resonators as tunable metamaterial components. J. Appl. Phys.. 2007;**101**:024911.

[17] T. H. Hand and S. A. Cummer. Frequency tunable electromagnetic metamaterial using ferroelectric loaded split rings. J. Appl. Phys. 2008;**103**:066105.

[18] H. Chen, B. I. Wu, L. Ran, et al. Controllable left-handed metamaterial and its application to a steerable antenna. Appl. Phys. Lett. 2006;**89**:053509.

[19] I. V. Shadrivov, S. K. Morrison, Y. S. Kivshar. Tunable split-ring resonators for nonlinear negative-index metamaterials. Opt. Express. 2006;**14**:9344–9349.

[20] Q. Zhao, L. Kang, B. Li, et al. Tunable negative refraction in nematic liquid crystals. Appl. Phys. Lett. 2006;**89**:221918.

[21] L. Kang, Q. Zhao, B. Li, et al. Experimental verification of a tunable optical negative refraction in nematic liquid crystals. Appl. Phys. Lett. 2007;**90**:181931.

[22] F. Zhang, Q. Zhao, L. Kang, et al. Magnetic control of negative permeability metamaterials based on liquid crystals. Appl. Phys. Lett. 2008;**90**:193104.

[23] F. Zhang, L. Kang, Q. Zhao, et al. Magnetically tunable left handed metamaterials by liquid crystal orientation. Opt. Express. 2009;**17**:4360–4366.

[24] Q. Zhao, L. Kang, B. Du, et al. Electrically tunable negative permeability metamaterials based on nematic liquid crystals. Appl. Phys. Lett. 2007;**90**:011112.

[25] D. H. Werner, D. H. Kwon, I. C. Khoo, et al. Liquid crystal clad near-infrared metamaterials with tunable negative-zero-positive refractive indices. Opt. Express. 2007;**15**:3342–3347.

[26] A. Minovich, D. N. Neshev, D. A. Powell, et al. Tunable fishnet metamaterials infiltrated by liquid crystals. Appl. Phys. Lett. 2010;**96**:193103.

[27] M. C. Ricci, H. Xu, R. Prozorov, et al. Tunability of superconducting metamaterials. IEEE Trans. Appl. Superconductivity. 2007;**17**:918–921.

[28] H. Tao, A. C. Strikwerda, K. Fan, et al. MEMS based structurally tunable metamaterials at terahertz frequencies. J. Infrared Milli. Terahz. Waves. 2011;**32**:580–595.

[29] M. Lapine, D. Powell, M. Gorkunov, et al. Structural tunability in metamaterials. Appl. Phys. Lett. 2009;**95**:084105.

[30] E. Ekmekci, A. C. Strikwerda, K. Fan, et al. Frequency tunable terahertz metamaterials using broadside coupled split-ring resonators. Phys. Rev. B. 2011;**83**:193103.

[31] G. Dewar. A thin wire array and magnetic host structure with n < 0. J. Appl. Phys. 2005;**97**:10Q101.

[32] G. Dewar. Minimization of losses in a structure having a negative index of refraction. New J. Phys. 2005;**7**:161.

[33] F. J. Rachford, D. N. Armstead, V. G. Harris, et al. Simulations of ferrite-dielectric-wire composite negative index materials. Phys. Rev. Lett. 2007;**99**:057202.

[34] X. B. Cai, X. M. Zhou, and G. K. Hu. Numerical study on left-handed materials made of ferrite and metallic wires. Chin. Phys. Lett. 2005;**23**:348–351.

[35] Y. He, P. He, S. D. Yoon, et al. Tunable negative index metamaterial using yttrium iron garnet. J. Magnetism Magnetic Mater. 2007;**313**:187–191.

[36] H. Zhao, J. Zhou, Q. Zhao, et al. Magnetotunable left-handed material consisting of yttrium iron garnet slab and metallic wires. Appl. Phys. Lett. 2007;**91**:131107.

[37] Y. J. Cao, G. J. Wen, K. M. Wu, et al. A novel approach to design microwave medium of negative refractive index and simulation verification. Chin. Sci. Bull. 2007;**52**:433–439.

[38] Y. Huang, G. Wen, T. Li, et al. Low-loss, broadband and tunable negative refractive index metamaterial. J. Electromag. Ana. Appl. 2010;**2**:104–110.

[39] L. Kang, Q. Zhao, H. Zhao, et al. Magnetically tunable negative permeability metamaterial composed by split ring resonators and ferrite rods. Opt. Express. 2008;**16**:8825–8834.

[40] L. Kang, Q. Zhao, H. Zhao, et al. Ferrite-based magnetically tunable left-handed metamaterial composed of SRRs and wires. Opt. Express. 2008;**16**:17269–17275.

[41] Y. J. Huang, G. J. Wen, Y. J. Yang, et al. Tunable dual-band ferrite-based metamaterials with dual negative refractions. Appl. Phys. A. 2012;**106**:79–86.

[42] K. Bi, J. Zhou, H. Zhao, et al. Tunable dual-band negative refractive index in ferrite-based metamaterials. Optics Express. 2013;**21**:10746–10752.

[43] B. Lax and K. J. Button. Microwave Ferrites and Ferrimagnetics. New York: McGraw-Hill; 1962.

[44] J. Zhou, L. Zhang, G. Tuttle, et al. Negative index materials using simple short wire pairs. Phys. Rev. B. 2006;**73**:041101.

[45] J. Huangfu, L. Ran, H. Chen, et al. Experimental confirmation of negative refractive index of a metamaterial composed of Ω-like metallic patterns. Appl. Phys. Lett. 2004;**84**:1537–1539.

[46] D. R. Smith, D. C. Vier, T. Koschny, et al. Electromagnetic parameter retrieval from inhomogeneous metamaterials. Phys. Rev. E. 2005;**71**:036617.

[47] E. Ekmekci and G. Turhan-Sayan. Single-loop resonator: dual-band magnetic metamaterial structure. Electron. Lett.. 2010;**46**:324–325.

[48] J. Zhong, F. Wang, G. Wen, et al. Tunable triple-band negative permeability metamaterial consisting of single-loop resonators and ferrite. J. Electromag. Waves Applicat. 2013;**27**:267–275.

[49] Y. J. Huang, G. J. Wen, and T. Q. Li, et al. Design and characterization of tunable terahertz metamaterials with broad bandwidth and low loss. IEEE Antennas Wireless Propagat. Lett. 2012;**11**:264–267.

[50] Q. H. Yang, H. W. Zhang, Y. L. Liu, Q. Y. Wen, and J. Zha. An artificially garnet crystal materials using in terahertz waveguide. Chin. Phys. Lett.. 2008;**25**:3957–3960.

[51] M. Walther, A. Ortner, H. Meier, U. Löffelmann, P. J. Smith, and J. G. Korvink. Terahertz metamaterials fabricated by inkjet printing. Appl. Phys. Lett.. 2008;**95**:251107.

[52] N. I. Landy, S. Sajuyigbe, J. J. Mock, D. R. Smith, and W. J. Padilla. Perfect metamaterial absorber. Phys. Rev. Lett. 2008;**100**:207402.

[53] X. Liu, T. Tyler, T. Starr, A. F. Starr, N. M. Jokerst, and W. J. Padilla. Taming the blackbody with infrared metamaterials as selective thermal emitters. Phys. Rev. Lett. 2011;**107**:045901.

[54] M. Yin, X. Y. Tian, L. L. Wu, and D. C. Li. A broadband and omnidirectional electromagnetic wave concentrator with gradient woodpile structure. Opt. Express. 2013;**21**:19082–19090.

[55] W. Withayachumnankul, H. Lin, K. Serita, C. M. Shah, S. Sriram, M. Bhaskaran, M. Tonouchi, and C. Fumeaux. Sub-diffraction thin-film sensing with planar terahertz metamaterials. Opt. Express. 2012;**20**:3345–3352.

[56] W. Zhu and X. Zhao. Metamaterial absorber with random dendritic cells. Eur. Phys. J. Appl. Phys. 2010;**50**:21101.

[57] J. Grant, Y. Ma, S. Saha, A. Khalid, and D. R. S. Cumming. Polarization insensitive, broadband terahertz metamaterial absorber. Opt. Lett. 2012;**36**:3476–3478.

[58] L. Huang, D. R. Chowdhury, S. Ramani, M. T. Reiten, S.-N. Luo, A. J. Taylor, and H.-T. Chen. Experimental demonstration of terahertz metamaterial absorbers with a broad and flat high absorption band. Opt. Lett. 2012;**37**:154–156.

[59] W. Zhu and X. Zhao. Metamaterial absorber with dendritic cells at infrared frequencies. J. Opt. Soc. Am. B. 2009;**26**:2382–2385.

[60] K. B. Alici, A. B. Turhan, C. M. Soukoulis, and E. Ozbay. Optically thin composite resonant absorber at the near-infrared band: A polarization independent and spectrally broadband configuration. Opt. Express. 2011;**19**:14260–14267.

[61] Q.-Y. Wen, Y.-S. Xie, H.-W. Zhang, Q.-H. Yang, Y.-X. Li, and Y.-L. Liu. Transmission line model and fields analysis of metamaterial absorber in the terahertz band. Opt. Express. 2009;**17**:20256–20265.

[62] H.-T. Chen. Interference theory of metamaterial perfect absorbers. Opt. Express. 2012; **20**:7165–7172.

[63] T. Wanghuang, W. Chen, Y. Huang, and G. Wen. Analysis of metamaterial absorber in normal and oblique incidence by using interference theory. AIP Adv. 2013;**3**:102118.

[64] Y. Pang, H. Cheng, Y. Zhou, and J. Wang. Analysis and design of wire-based metamaterial absorbers using equivalent circuit approach. J. Appl. Phys. 2013;**113**:114902.

[65] J. Zhong, Y. Huang, G. Wen, H. Sun, P. Wang, and O. Gordon. Single-/dual-band metamaterial absorber based on cross-circular-loop resonator with shorted stubs. Appl. Phys. A. 2012;**108**:329–335.

[66] Y. Huang, Y. Tian, G. Wen, and W. Zhu. Experimental study of absorption band controllable planar metamaterial absorber using asymmetrical snowflake-shaped configuration. J. Opt. 2013;**15**:055104.

[67] H. Li, L. H. Yuan, B. Zhou, X. P. Shen, Q. Cheng, and T. J. Cui. Ultrathin multiband gigahertz metamaterial absorbers. J. Appl. Phys. 2011;**110**:014909.

[68] J. Sun, L. Liu, G. Dong, and J. Zhou. An extremely broad band metamaterial absorber based on destructive interference. Opt. Express. 2011;**19**:21155–21162.

[69] Y. Cui, K. H. Fung, J. Xu, H. Ma, Y. Jin, S. He, and N. X. Fang. Ultrabroadband light absorption by a sawtooth anisotropic metamaterial slab. Nano Lett. 2012;**12**:1443–1447.

[70] J. Zhao, Q. Cheng, J. Chen, M. Q. Qi, W. X. Jiang, and T. J. Cui. A tunable metamaterial absorber using varactor diodes. New J. Phys. 2013;**15**:043049.

[71] D. Shrekenhamer, W.-C. Chen, and W. J. Padilla. Liquid crystal tunable metamaterial absorber. Phys. Rev. Lett. 2013;**110**:177403.

[72] A. Andryieuski and A. V. Lavrinenko. Graphene metamaterials based tunable terahertz absorber: Effective surface conductivity approach. Opt. Express. 2013;**21**:9144–9155.

[73] T. Cao, L. Zhang, R. E. Simpson, and M. J. Cryan. Mid-infrared tunable polarization-independent perfect absorber using a phase-change metamaterial. J. Opt. Soc. Am. B. 2013;**30**:1580–1585.

[74] Q.-Y. Wen, H.-W. Zhang, Q.-H. Yang, Z. Chen, Y. Long, Y.-L. Jing, Y. Lin, and P.-X. Zhang. A tunable hybrid metamaterial absorber based on vanadium oxide films. J. Phys. D: Appl. Phys. 2012;**45**:235106.

[75] A. Moreau, C. Ciracı, J. J. Mock, R. T. Hill, Q. Wang, B. J. Wiley, A. Chilkoti, and D. R. Smith. Controlled-reflectance surfaces with film-coupled colloidal nanoantennas. Nature (London). 2012;**492**:86–90.

[76] W. Zhu, Y. Huang, I. D. Rukhlenko, G. Wen, and M. Premaratne. Configurable metamaterial absorber with pseudo wideband spectrum. Opt. Express. 2012;**20**:6616–6621.

[77] Y. J. Yang, Y. J. Huang, G. J. Wen, J. P. Zhong, H. B. Sun, and O. Gordon. Tunable broadband metamaterial absorber consisting of ferrite and wire. Chin. Phys. B. 2012;**21**:038501.

[78] Y. Huang, G. Wen, W. Zhu, J. Li, L.-M. Si, and M. Premaratne. Experimental demonstration of a magnetically tunable ferrite based metamaterial absorber. Opt. Express. 2014;**22**:16408–16417.

IntechOpen